Wei Liu · Siming He

Influence of runoff on debris flow propagation at a catchment scale: a case study

Abstract Debris flow mobility can vary during propagation due to changes in flow volume and bulk flow behavior resulting from the absorption of water from runoff. This study aims to investigate the effect of runoff on debris flow propagation by presenting an integrated model that considers the processes of rainfall, vegetation interception, soil infiltration, runoff generation, and debris flow propagation. Specifically, the study adopts an elevation-based empirical formula to evaluate the spatial distribution of rainfall and introduces a parameter for water absorption rate into the depth-averaged two-layer model that is used for describing the dynamics of runoff and debris flow. Through alternative simulations of the 2020 debris flow in the Meilong catchment, the study illustrates the significant effects of water absorption on debris flow propagation. The results indicate that as the water absorption rate of the debris mass increases, debris flow mobility also increases, since more mass and energy are transferred from runoff to debris flow. In addition, the spatial and temporal patterns of rainfall intensity can modify the propagation velocity of debris flow by influencing runoff dynamics.

Keywords Debris flow mobility · Runoff generation · Water absorption · Numerical modeling · Rainfall variability

Introduction

Debris flows are a typical mountain disaster and can result in high casualties or serious economic loss due to its large impact area and great destructive power (Norio et al. 2011). Recent examples include the 2010 Hongchun debris flow, which resulted in the flooding of Yingxiu town (Tang et al. 2011), and the 2010 Tianmo debris flow, which blocked Parlung Zangbo River and caused a direct loss of CNY 5.2 million (Wei et al. 2018). Generally, the impact area and impact force of debris flows are significantly correlated to their mobility. Based on the analysis of available data (e.g., the ratio between drop height and runout distance), several studies have demonstrated that there is a significant variation in the mobility of debris flows (Dahlquist and West 2019; Rickenmann 1999; Tang et al. 2012a, b). Consequently, understanding the factors that affect the mobility of debris flows, and the extent to which they do so, is critical for evaluating disaster risk and informing reconstruction strategies.

Debris flow mobility may vary during propagation through the channel due to changes in flow volume and bulk flow behavior caused by entrainment of bed sediments and water absorption from runoff (Rickenmann and Scheidl 2012). To date, how sediment entrainment affects debris flow mobility has been studied deeply through laboratory experiments (Iverson et al. 2010; Reid et al. 2011) and theoretical analysis (Frank et al. 2019; Luna et al. 2012). Based on

the large flux experiments, Iverson et al. (2011) found that a debris flow over a fixed wet bed moves significantly faster than the same flow over a fixed dry bed. McCoy et al. (2012) measured bed and flow properties during six erosive debris flow events and discovered that the eroded mass from debris flow is also larger when the bed sediment is saturated compared to dry bed sediment. To describe debris flow propagation under the effects of sediment entrainment quantitatively, several physically based numerical models have also been proposed, based on the depth-averaged theory (Frank et al. 2019; Han et al. 2015). Luna et al. (2012) coupled a one-dimensional debris flow model with an erosion formula that considered the limit equilibrium and excess pore water pressure of bed materials. Discussion on the mass and momentum jump conditions that impose constraints on valid erosion formulas was performed by Iverson and Ouyang (2015), which provides a guideline for applying correct forms of depth-averaged equations considering entrainment. Compared to the entrainment mechanism and its effects on debris flow mobility, the study of water absorption during debris flow propagation is rare. Debris flows can absorb water from runoff when they meet and change their volume and bulk flow behavior, which changes the mobility (Rickenmann and Scheidl 2012). Moreover, water absorption can also transfer momentum from runoff to debris flows, which is different from sediment entrainment due to that the sediment should be static prior to entrainment (Han et al. 2015). For catchments with steep terrain or heavy rainfall, runoff may have large kinetic energy and transfer it to debris flow through water absorption, thus promoting debris flow propagation (Pierson and Scott 1985). However, there are no available numerical models that incorporate the abovementioned effects of water absorption on debris flow propagation, especially from the catchment point of view.

The spatial heterogeneity of rainfall intensity, an important feature for rainfall events in mountainous areas, significantly influences hydrological processes and thus increases the susceptibility to disasters (Minder et al. 2009; von Ruette et al. 2014). Obtaining accurate rainfall data in catchments is challenging due to harsh monitoring conditions or measurement errors, particularly for high-altitude areas. Moreover, the relationship between elevation and rainfall in small-scale spaces, such as single catchments, is complex and highly uncertain (Haiden and Pistotnik 2009). Several formulas have been proposed to estimate this relationship, primarily based on regional rainfall data (Garcia-Martino et al. 1996; Guo et al. 2021; Jiang et al. 1988; Song et al. 2019). These formulas generally follow a simple rule whereby rainfall intensity initially increases with elevation and then decreases. Currently, rainfall data available for a catchment typically comes from the nearest meteorological station, which

represents an average of the entire area and provides a general reference to simulate rainfall conditions. The high spatial variability of rainfall introduces uncertainty in predicting runoff generation, including characteristics such as volume and peak discharge (Bout et al. 2018; Liu and He 2020). In order to improve the accuracy of simulating runoff in a catchment, An et al. (2022) used rainfall data with spatial variation, which was obtained by interpolating data from 17 meteorological stations located nearby. However, since these stations are not located within the catchment and most of them are far away, there is a possibility that the impact of changes in elevation on the rainfall data may be overlooked. Currently, employing an empirical formula that links rainfall intensity and elevation is an effective method for enhancing the accuracy of simulating runoff generation within a catchment. However, studies on the application of this method to simulate debris flow formation are scarce.

In this paper, a multi-process coupling model is introduced to assess the impact of water absorption on debris flow propagation at a catchment scale. To account for the significant spatial heterogeneity of rainfall in mountainous regions due to varying elevations, an elevation-based empirical formula is incorporated into the model to calculate the spatial distribution of rainfall. Additionally, models of vegetation interception and soil infiltration are coupled with the model as these processes play a crucial role in the overall dynamics. Furthermore, a depth-averaged two-layer model that includes a newly introduced parameter of water absorption rate is proposed to effectively simulate the behavior of runoff and debris flow, as well as their interaction. To validate the presented model, it is applied to a debris flow event that took place in Meilong catchment, China, in 2020. Various alternative scenarios are simulated to investigate the sensitivities of water absorption rate and rainfall intermittency to debris flow propagation.

Numerical framework

Rainfall-runoff processes are impacted by a wide range of processes including variability of the rainfall, interception, and infiltration (refer to Fig. 1). When the runoff encounters a debris mass along its path, it has the potential to be absorbed, thereby modifying the characteristics of the debris mass, such as the solid-liquid ratio and subsequently its mobility (Rickenmann and Scheidl 2012). Considering this perspective, for a numerical model investigation of the impact of rainfall-runoff on debris flow propagation at a catchment scale, two critical issues need to be addressed: obtaining accurate runoff results by considering the aforementioned factors and appropriately incorporating the interaction between runoff and the debris mass. To tackle these challenges, we integrate the models for the relevant processes and introduce a parameter to quantitatively describe the absorption of water from runoff by the debris flow.

Coupled models for calculating effective precipitation contributed to runoff

Effective precipitation varies as a function of vegetation interception and surface infiltration (Das et al. 2006), but in this study, we focus on the following processes because it is influenced by factors such as the rainfall pattern and vegetation coverage and type. From this point of view, we couple existing physical-based models that incorporate these factors to quantitatively describe the amount of effective precipitation that contributes to runoff (see Fig. 2). We define the effective precipitation as parameter I, which is expressed as follows:

$$I = I_a - \Delta I_c - I_f \tag{1}$$

where I_a is the initial rainfall intensity; ΔI_c and I_f are the interception loss rate and infiltration loss rate per time unit, respectively.
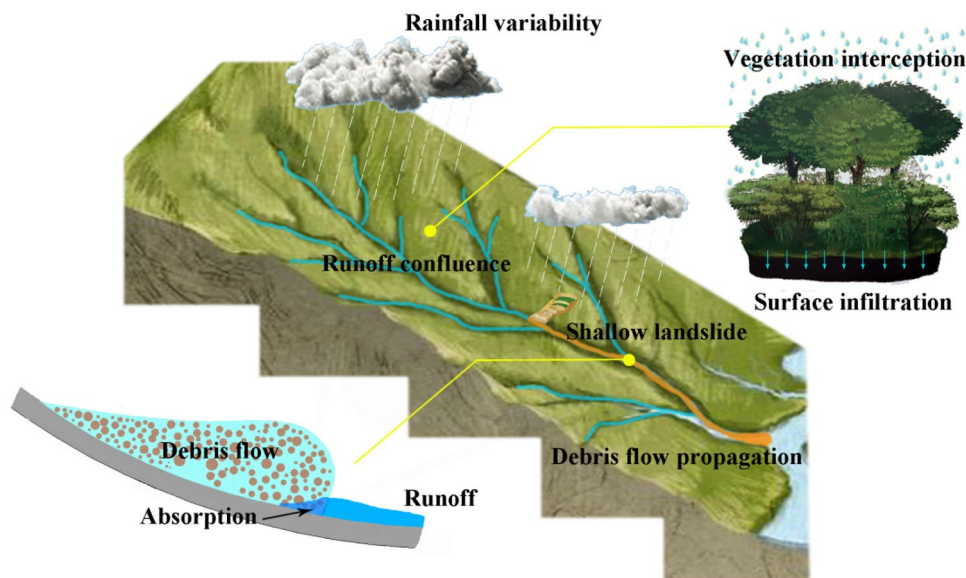

Fig. 1 Sketch of runoff generation under the coupling action of rainfall variability, vegetation interception, and surface infiltration and its effect on debris flow propagation
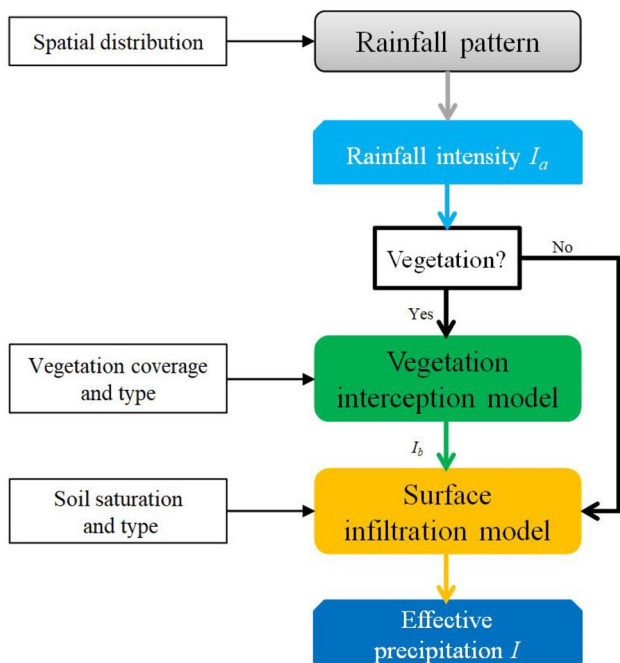
Fig. 2 Flowchart of effective precipitation calculation by coupling models of rainfall pattern, vegetation interception, and surface infiltration. Here, $I_b = I_a - \Delta I_c$ refers to the effective precipitation after vegetation interception

Rainfall spatial distribution model

A formula that reflects this simple relationship between elevation and rainfall is expressed as (Jiang et al. 1988)

$$I_a = Ae^{-B(z-H)^2} + C \tag{2}$$

where z is the elevation; H is the elevation which has the maximum rainfall intensity; A and B are the empirical parameters; C is the reference rainfall intensity when z becomes large and is usually assumed to be zero.

Vegetation interception model

Aston (1979) proposed an empirical formula for describing interception

$$I_c = S_{max}\left[1 - \exp\left(-\frac{kP_t}{S_{max}}\right)\right] \tag{3}$$

which I_c is the accumulated interception loss; P_t is the accumulated rainfall; $k = 0.046 \cdot LAI$ is a correction factor, in which LAI is leaf area index; S_{max} is the maximum canopy storage and varies with land covers (von Hoyningen-Huene 1983)

$$S_{max} = \begin{cases} 0.2856 LAI & \text{for forest} \\ 0.935 + 0.948 LAI - 0.00575 LAI^2 & \text{for cultivated land} \\ 0.59 LAI^{0.88} & \text{for grassland} \end{cases} \tag{4}$$

Soil infiltration model

Soil infiltration here is described by one-dimensional Richard's equation (Swartzendruber 1987)

$$\frac{\partial \theta}{\partial t} = \frac{\partial}{\partial z}\left(D\frac{\partial \theta}{\partial z} - K\right) - S \tag{5}$$

where z is the depth from the soil surface (taken the upward direction as positive); θ is the soil water content; D is the hydraulic diffusivity; K is the hydraulic conductivity; $S = \chi \cdot \varsigma \cdot T_p$ is the water sink term by plant root (Zhu et al. 2018); χ is the root distribution function, and here, a linearly decreasing distribution (Prasad 1988) is applied to all plants with different maximum root lengths; T_p is the maximum transpiration rate; ς is the transpiration reduction function and assumed to be 1 for simplicity. To solve Eq. (5), Neumann and Dirichlet conditions are applied in the upper and lower boundaries of soil, respectively.

$$\begin{cases} -D\frac{\partial \theta}{\partial z} + K = I_f & \text{upper boundary} \\ \theta = \theta_i & \text{lower boundary} \end{cases} \tag{6}$$

where θ_i is the initial soil water content.

Depth-averaged model for calculating runoff and debris flow propagation

Conservation equations

Previous research has demonstrated the effectiveness of depth-averaged models in capturing the dynamics of both runoff (Singh et al. 2015; Caviedes-Voullième et al. 2012) and debris flow (Medina et al. 2008; Pudasaini et al. 2005; Rengers et al. 2016). Field observations and experimental evidence have shown that saturated materials from shallow landslides can quickly transition into debris flows (Fleming et al. 1989; Iverson et al. 1997). However, considering the intricate nature of this transformation process and its short duration compared to the entire event, we simplify the model by disregarding this process and treating the collapsed mass as debris flow directly. It is important to note that this simplification may introduce inaccuracies in the initial state of debris flow propagation. When debris flow interacts with runoff, the different densities of the two layers enable the consideration of a typical two-layer problem using two-layer models (Bouchut et al. 2016; Chen and Peng 2006; Liu and He 2018; Meyart et al. 2022). However, although some two-layer models have attempted to model the entrainment between debris flow and the bed, they do not typically account for the addition of water to the debris. In our study, we assume that the mixture component belongs to the debris flow, resulting in the existence of an interface boundary that separates pure water flow from debris flows. To incorporate this concept, we introduce a parameter that characterizes the absorption rate of pure water into the debris mass. This new parameter is integrated into a two-layer depth-averaged model, enabling the replication of runoff/debris flow propagation at the catchment scale. The derivation of the model equations based on depth-averaged theory is presented in the Appendix. The derivation process in this study is similar to that presented in previous studies (Iverson and Ouyang 2015; Liu and He 2016). However, in the model equations, new terms have been introduced to account for the effect of water absorption on the mass and momentum of each layer. By assuming a lateral stress coefficient $k_{ap} = 1$ for debris flow, as proposed by George and Iverson (2014), the two-layer depth-averaged model is expressed in the Cartesian coordinate system as follows:

$$\frac{\partial h_1}{\partial t} + \frac{\partial}{\partial x}\left(h_1 u_1\right) + \frac{\partial}{\partial y}\left(h_1 v_1\right) = I - E_m \tag{7-1}$$

$$\frac{\partial}{\partial t}\left(h_1 u_1\right) + \frac{\partial}{\partial x}\left(h_1 u_1^2 + \tfrac{1}{2}g h_1^2\right) + \frac{\partial}{\partial y}\left(h_1 u_1 v_1\right) = -u_1(z_m)E_m - g h_1 \frac{\partial}{\partial x}\left(z_b + h_2\right) - \tau_{s1x} \tag{7-2}$$

$$\frac{\partial}{\partial t}\left(h_1 v_1\right) + \frac{\partial}{\partial x}\left(h_1 u_1 v_1\right) + \frac{\partial}{\partial y}\left(h_1 v_1^2 + \tfrac{1}{2}g h_1^2\right) = -v_1(z_m)E_m - g h_1 \frac{\partial}{\partial y}\left(z_b + h_2\right) - \tau_{s1y} \tag{7-3}$$

$$\frac{\partial h_2}{\partial t} + \frac{\partial}{\partial x}\left(h_2 u_2\right) + \frac{\partial}{\partial y}\left(h_2 v_2\right) = \gamma_m E_m + E_b \tag{8-1}$$

$$\frac{\partial}{\partial t}\left(h_2 u_2\right) + \frac{\partial}{\partial x}\left(h_2 u_2^2 + \tfrac{1}{2}g h_2^2 + \gamma_m g h_1 h_2\right) + \frac{\partial}{\partial y}\left(h_2 u_2 v_2\right) = u_1(z_m)\gamma_m E_m + u_2(z_b)E_b \\ + \gamma_m g h_1 \frac{\partial h_2}{\partial x} - g h_2 \frac{\partial z_b}{\partial x} + \gamma_m \tau_{s1x} - \tau_{s2x} \tag{8-2}$$

$$\frac{\partial}{\partial t}\left(h_2 v_2\right) + \frac{\partial}{\partial x}\left(h_2 u_2 v_2\right) + \frac{\partial}{\partial y}\left(h_2 v_2^2 + \tfrac{1}{2}g h_2^2 + \gamma_m g h_1 h_2\right) = v_1(z_m)\gamma_m E_m + v_2(z_b)E_b + \gamma_m g h_1 \frac{\partial h_2}{\partial y} - g h_2 \frac{\partial z_b}{\partial y} + \gamma_m \tau_{s1y} - \tau_{s2y} \tag{8-3}$$

$$\frac{\partial\left(h_2 c_d\right)}{\partial t} + \frac{\partial\left(h_2 u_2 c_d\right)}{\partial x} + \frac{\partial\left(h_2 u_2 c_d\right)}{\partial y} = \left(1 - p\right)E_b \tag{8-4}$$

$$\frac{\partial z_b}{\partial t} = -E_b \tag{9}$$

where t is the time; h_1 and h_2 are the depth of runoff and debris flow respectively; the two fluids, runoff and debris flow, have distinct densities γ_1 and $\gamma_2 = c_d \gamma_s + (1-c_d)\gamma_f$, with corresponding velocities $\mathbf{u}_1 = (u_1, v_1)$ and $\mathbf{u}_2 = (u_2, v_2)$, respectively; c_d is the depth-averaged solid volume fraction; γ_s and γ_f are the densities of dry soil and fluid contributed into debris flow, respectively, and here $\gamma_1 = \gamma_f$; z_b is the bed surface elevation; $\gamma_m = \gamma_1/\gamma_2$ is the density ratio between runoff and debris flow; $\tau_{s1} = g_z n_b^2/h_1^{1/3}(\mathbf{u}_1 - \mathbf{u}_2)|\mathbf{u}_1 - \mathbf{u}_2|$ refers to the shear stress at the interface between debris flow and runoff, which obeys Manning frictional law; n_b is the Manning roughness coefficient and g_z the gravity acceleration; the shear stress from debris flow $\tau_{s2} = c_d g_z h_2(1-\gamma_m)\tan\varphi_{bed} + (1-c_d)g_z n_b^2/h_2^{1/3}|\mathbf{u}_2|\,\mathbf{u}_2|$ (Liu and He 2020; An et al. 2022), in which φ_{bed} is the basal frictional angle; E_m is the absorption rate of water from runoff by debris mass when they meet; $\mathbf{u}_{1m} = (u_{1m}, v_{1m})$ and $\mathbf{u}_{2b} = (u_{1b}, v_{1b})$ is the velocities for the flows at the interface boundary. In the following, it is assumed that the velocities on the interface between runoff and debris flow are equal to the depth-averaged one, $\mathbf{u}_{1m} = \mathbf{u}_1$ and the velocities on the interface between debris flow and channel bed are equal to zero, $\mathbf{u}_{2b} = 0$ (Han et al. 2015); p is the sediment porosity; E_b is the erosion rate between debris flow and bed surface.

To summarize, the conservation of mass for runoff and debris flow is represented by Eqs. (7-1) and (8-1), while the conservation of momentum for runoff and debris flow in the x and y directions is represented by Eqs. (7-2), (7-3), (8-2), and (8-3). In the runoff momentum equations, the right side terms correspond to mass transfer, topography, and friction loss. Similarly, in the debris flow momentum equations, the right side terms correspond to mass transfer, interactive force, topography, and friction loss. Equation (9) represents the mass conservation of bed sediments. The structure of Eqs. (7) and (8) can be viewed as a typical

two-layer model when assuming $E_m = 0$. This situation arises when the debris mass has high viscosity and only briefly interacts with runoff. Alternatively, Eqs. (7) and (8) can be simplified by assuming certain terms equal to zero. For example, $h_2 = 0$ in Eqs. (7-2) and (7-3), and $h_1 = 0$ and $\tau_{s1} = 0$ in Eqs. (8-2) and (8-3). This simplification assumes that runoff can be instantaneously absorbed by debris flow upon contact, with E_m equal to h_1.

This model offers two key advantages. Firstly, it considers the effects of rainfall spatial distribution, vegetation interception, and surface infiltration on the generation of runoff. Secondly, it enables the simultaneous description of the propagation of runoff and debris flow, their interaction, and the erosion effects of sediment. Utilizing this numerical framework allows for obtaining the characteristics of runoff/debris flow evolution, such as depth, velocity, solid volume fraction, and the associated erosion rate at each time step. Consequently, it facilitates the analysis of how the characteristics of catchment runoff affect the propagation of debris flow.

Model closure
Determining the value of E_m significantly impacts the mass transformation between the two flows and, in turn, the propagation of debris flow. E_m will vary during debris flow propagation, depending on flow velocity, flow density, and flow viscosity (Mohrig and Marr 2003; Talling et al. 2002). However, we note that there is currently no available formula for evaluating E_m. In the study conducted by Talling et al. (2002), both experimental investigations and theoretical analysis were employed to examine the rates and processes of mixing between debris mass and water in the context of submarine debris flows. The authors emphasized the significance of shear mixing in facilitating the incorporation of water into the debris mass. Additionally, Talling et al. (2002) emphasized that the flow viscosity, which is influenced by the grain component and gradation of the debris, has a substantial impact on the rate of mixing. Similar results have also been found in Mohrig and Marr (2003) and Yin and Rui (2018). Their findings indicate that the mixture rates differ for weak and strong debris materials, ranging from 0.00001 to 100 m/min. From this, we make the assumption that, for the sake of simplification, the value of E_m remains constant within this range throughout the simulation.

The value of E_b is commonly understood to be determined by the imbalance between the upper shear stress and the lower shear resistance (Fraccarollo and Capart 2002; Iverson and Ouyang 2015; Medina et al. 2008). Consequently, this relationship can be expressed as follows (Iverson and Ouyang 2015; Liu et al. 2015):

$$E_b = \frac{\left(\gamma_2|\boldsymbol{\tau}_{s2}| - \tau_{b2}\right)}{\gamma_2|\mathbf{u}_2|}\left(1 - e^{-\varepsilon|u_2|^2}\right) \tag{10}$$

where ε is a calibrated erosion coefficient; the bed shear resistance $\tau_{b2} = c_m + (1-\lambda)\gamma_2 g_z h_2 \tan\varphi_{int}$, in which c_m is the cohesion of sediment materials, and λ is the pore pressure ratio that indicates the degree of liquefaction of the bed material; φ_{int} is the internal friction angle of sediment materials.

Computing method

The specific details of the numerical method employed to solve the model equations mentioned above have been extensively documented in other works (Liang and Marche 2009; Liu and He 2020). Hence, only a concise summary of the key elements of the approach will be provided here. To begin with, we employ the finite volume method to solve Eqs. (2), (3), and (5) in order to obtain the values of I_a, ΔI_c, and I_f and further obtain the value of I by solving Eq. (1) (see the iterative process illustrated in Fig. 1). Subsequently, we utilize this calculated data to solve Eqs. (7)–(9), which are also discretized using the finite volume method on a rectangular grid arrangement as described below.

$$\frac{\partial \mathbf{U}}{\partial t} + \frac{\partial \mathbf{F}}{\partial x} + \frac{\partial \mathbf{G}}{\partial y} = \mathbf{S} + \mathbf{T} \tag{11}$$

where $\mathbf{U}$, $\mathbf{F}$, $\mathbf{G}$, $\mathbf{S}$, and $\mathbf{T}$ are vectors representing the variables conserved, the fluxes in the x and y directions, and the source terms in the x and y directions, respectively.

$$\mathbf{U} = \begin{pmatrix} h_1 \\ h_1 u_1 \\ h_1 v_1 \\ h_2 \\ h_2 u_2 \\ h_2 v_2 \\ h_2 c_d \\ z_b \end{pmatrix}, \mathbf{F} = \begin{pmatrix} h_1 u_1 \\ h_1 u_1^2 + \frac{1}{2} g h_1^2 \\ h_1 u_1 v_1 \\ h_2 u_2 \\ h_2 u_2^2 + \frac{1}{2} g h_2^2 + \gamma_m g h_1 h_2 \\ h_2 u_2 v_2 \\ h_2 u_2 c_d \\ 0 \end{pmatrix}, \mathbf{G} = \begin{pmatrix} h_1 v_1 \\ h_1 u_1 v_1 \\ h_1 v_1^2 + \frac{1}{2} g h_1^2 \\ h_2 v_2 \\ h_2 u_2 v_2 \\ h_2 v_2^2 + \frac{1}{2} g h_2^2 + \gamma_m g h_1 h_2 \\ h_2 v_2 c_d \\ 0 \end{pmatrix},$$

$$\mathbf{S} = \begin{pmatrix} I - E_m \\ -u_1(z_m)E_m - gh_1\frac{\partial}{\partial x}(z_b + h_2) - \tau_{s1x} \\ 0 \\ \gamma_m E_m + E_b \\ u_1(z_m)\gamma_m E_m + u_2(z_b)E_b + \gamma_m g h_1 \frac{\partial h_2}{\partial x} \\ -gh_2\frac{\partial z_b}{\partial x} + \gamma_m \tau_{s1x} - \tau_{s2x} \\ 0 \\ (1-p)E_b \\ -E_b \end{pmatrix}, \mathbf{T} = \begin{pmatrix} 0 \\ 0 \\ -v_1(z_m)E_m - gh_1\frac{\partial}{\partial y}(z_b + h_2) - \tau_{s1y} \\ 0 \\ 0 \\ v_1(z_m)\gamma_m E_m + v_2(z_b)E_b + \gamma_m g h_1 \frac{\partial h_2}{\partial y} \\ -gh_2\frac{\partial z_b}{\partial y} + \gamma_m \tau_{s1y} - \tau_{s2y} \\ 0 \\ 0 \end{pmatrix}. \tag{12}$$

To ensure accuracy and efficiency, a fraction-step scheme with second-order accuracy is employed. The flux terms, $\mathbf{F}$ and $\mathbf{G}$, in the equations are calculated using the Harten-Lax-van Leer-Contact solver, while the partial differential terms are computed using a three-point central differencing scheme. To accurately capture the steady state behavior during the simulation of flows over complex domains with wetting and drying, the well-balanced finite volume approach proposed by Audusse et al. (2004) is employed. To ensure the numerical stability of the scheme, the Courant-Friedrichs-Lewy criterion is used to determine an appropriate time step. At this point, all the variables are updated by solving Eqs. (1), (2), (3), (5), and (7)–(9) at each time step. Notably, Eq. (8) is not computed until the time of landslide initiation is reached in order to reduce computational costs. The measured data concerning the mass of the landslide (volume, depth, and area) is directly assigned to h_2 for calculating debris flow propagation once the landslide occurs, as the process of slope instability is not considered in this study.

Modeling the dynamics of the 2020 Meilong debris flow

Overview of the event

Figure 3 shows the Meilong catchment, which experienced a debris flow event on June 17, 2020. This catchment has a drainage area of approximately 62.55 km², and its elevation ranges from 2116 to 4824 m above sea level (a.s.l). As recorded by the Banshanmen meteorological station that is located 3 km away from the Meilong catchment, a storm from 22:00 on June 16 to 03:30 on June 17 with an accumulated value of 34.4 mm served as the trigger for the debris flow (Fig. 3c). The debris flow was initiated by a shallow landslide with a volume of 4.2×10^4 m³ in the upstream section of the gully (Fig. 3d). Through the erosion of loose sediment materials along its path (Fig. 3e, f), the debris flow expanded to a volume of 4×10^5 m³ and flowed out of the valley around 03:10 (Zhao et al. 2021). Subsequently, the debris flow material swiftly obstructed the XJC River, forming a barrier dam with an estimated height ranging from 8 to 12 m (Fig. 3g). The bedrock in the Meilong catchment primarily comprises quartzite, marble, and slate.

Analysis of debris flow propagation

The runout distance L and drop height H of debris flow are approximately 1.08×10^4 m and 1740 m, respectively, based on the field investigation and interpretation with remote sensing technology. A small ratio of $H/L = 0.161$ indicates a high mobility of the debris flow compared to many other events (Dahlquist and West 2019; Tang et al. 2012a, b). We suspect this high mobility may be attributed to the steep terrain that has an average longitudinal gradient of 0.157 (Fig. 4a), as well as the entrainment that increases mass volume (Fig. 4b, c) and runoff that gives extra dynamics. Before the occurrence of the debris flow event, the Meilong catchment experienced continuous rainfall, accumulating a total precipitation of 107 mm from June 3rd to 14th, 2020, as recorded by rainfall data collected at the nearby Anianggouer station (Yan et al. 2021; Zhao et al. 2021). Local residents living near the gully entrance also reported a noticeable increase in runoff discharge prior to the debris flow event. Based on these observations, it is inferred that the aeration zone within the catchment reached saturation prior to the debris flow event, leading to a storage-excess runoff process in the catchment. Consequently, the rapid generation of runoff swiftly converges at the main gully, leading to the formation of a high-volume water flow, which creates favorable conditions for the development of debris flow when solid materials are introduced. This process is similar to the formation of a debris flood event, as described by Church and Jakob (2020).

Model parameters calibration

In order to ensure the reliability of the calculated results, calibration of model parameters is necessary. A summary of the parameter values utilized in the simulation is presented in Table 1. The values for the friction coefficient, phase density, saturation,
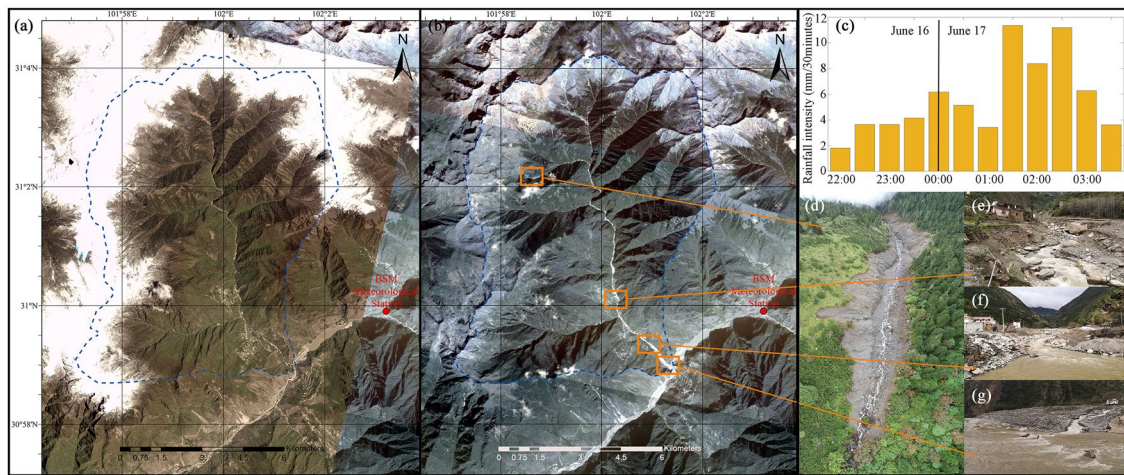
Fig. 3 Images of the Meilong catchment obtained by satellite and unmanned aerial vehicle (**a**) before the event and (**b**) after the event; (**c**) half-hourly rainfall intensity during the rainstorm, occurring from 22:00 on June 16 to 03:30 on June 17 and obtained from the Banshanmen meteorological station (marked by a red point); (**d**) the original shallow landslide; (**e**), (**f**) the downstream section of the gully eroded by the debris flow and (**g**) the fan-shaped debris deposits located at the gully outlet

and cohesion of sediment for the study site have been estimated through previous research (An et al. 2022; Jiang et al. 2022), which relied on literature, field investigations, and laboratory analyses. The digital elevation models (DEMs) used in this study, with a resolution of 10 m, were obtained from stereo images collected by the Chinese satellite Ziyuan-3. It is important to note that the Meilong catchment exhibits high vegetation coverage, which results in a noticeable reduction in runoff due to processes such as interception, evaporation, and infiltration. The Meilong catchment comprises various vegetation types, such as forest, grassland, and cultivated land (An et al. 2022). The spatial distribution of the leaf area index (LAI) for these vegetation types, with an accuracy of 10 m, was obtained through remote sensing interpretation using 250-m accuracy GLASS data and data interpolation (see Fig. 5a, b). The process of soil infiltration is not considered in this study, as the aeration zone in the catchment was assumed to be saturated prior to the occurrence of the debris flow. Yan et al. (2021) conducted an analysis of the seismic signals from the Meilong debris flow and proposed that the event initiation occurred around 02:50 on June 17, 2020. Empirical parameters, such as the altitude at which maximum rainfall intensity (H) occurs and the erosion coefficient (ε), are calibrated using a trial-and-error procedure to achieve a situation that closely matches reality. According to Hu et al. (2020), Yan et al. (2021), and Zhao et al. (2021), the maximum hourly rainfall intensity recorded by different meteorological station varies from 11.4 to 34.1 mm/h. Based on this data, Fig. 5c illustrates the spatial distribution of rainfall with an altitude (H) of 3600 m and an erosion coefficient (B) of 4.5×10^{-7}, corresponding to an intensity of 11.4 mm/h in the gully entrance and the maximum intensity of 34.1 mm/h within the catchment.
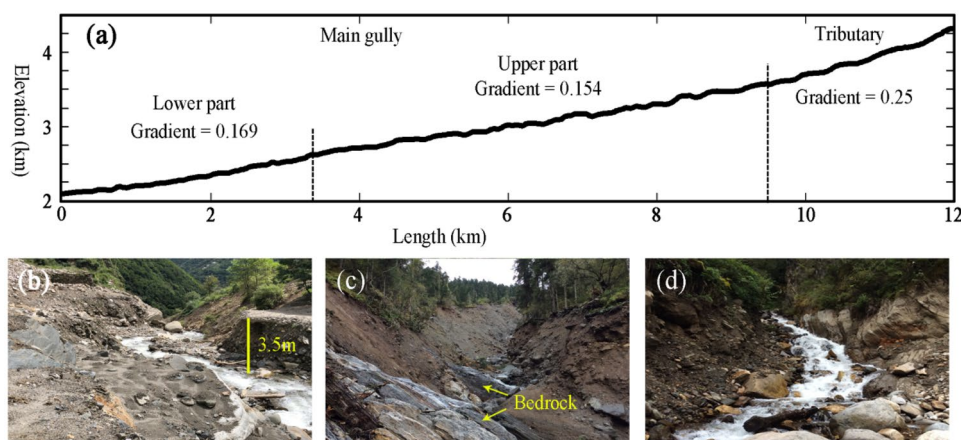

Fig. 4 a Profiles of the main gully and the tributary where landslide occurred; observed cross-sections of the lower part (**b**) and upper part (**c**) of main gully eroded by debris flow; **d** observed stream within the catchment

Table 1 Model parameter values used in simulation of the 2020 Meilong debris flow

Symbol	Unit	Definition	Value	Source
n_b	s/m$^{1/3}$	Manning coefficient	0.04	Jiang et al. (2022)
φ_{int}	°	Internal friction angle	30	An et al. (2022)
φ_{bed}	°	Basal friction angle	15	An et al. (2022)
B	–	Rainfall distribution coefficient	4.5×10^{-7}	Calibration
g	m/s^2	Gravity acceleration	9.8	Liu et al. (2015)
γ_s	kg/m^3	Density of dry soil	2650	An et al. (2022)
γ_f	kg/m^3	Density of pure water	1000	An et al. (2022)
ε	–	Erodibility coefficient	0.0006	Calibration
c_m	kPa	Cohesion of sediment materials	5	An et al. (2022)
λ	–	Pore pressure ratio of sediment materials	0.8	An et al. (2022)
p	–	Sediment porosity	0.4	Liu et al. (2020)
H	m	Altitude with maximum rainfall intensity	3600	Calibration
E_m	m/min	Water absorption rate	0.1	Talling et al. (2002)

Numerical results for alternative debris flow scenarios

To validate our approach for simulating runoff and debris flow propagation on a catchment scale, we first simulate the processes of runoff generation and debris flow propagation under non-uniform rainfall distribution and compare the results with findings from other studies and field observations. Before the occurrence of the shallow landslide in the upstream area of the gully, the modeled runoff had a high flow discharge of approximately 200 m³/s near the gully outlet (see Fig. 6a). This discharge was accompanied by a rainwater loss of 12.8% caused by vegetation interception. The simulated flow discharge value is higher than the value of approximately 100 m³/s calculated by An et al. (2022). This difference can be attributed to our smaller calculated rainwater loss value, which

is lower than the 22.5% calculated by An et al. (2022). An et al. (2022) used a large *LAI* value (~30.78) applied to the entire vegetated area in the catchment, resulting in higher rainwater loss. After the shallow landslide occurred, a debris flow formed, which then merged with runoff in the channel, increased in size via water absorption, and eroded the channel bed as a consequence of elevated shear stresses over a saturated substrate (refer to Figs. 6b, c and 7a). The debris flow reached the middle section of the gully, attaining a maximum flow depth of 8.6 m and a maximum velocity of 11.8 m/s, at 03:08. Subsequently, it reached the gully outlet, with a maximum flow depth of 9.2 m and a maximum velocity of 14.6 m/s, at 03:18. These arrival times are consistent with the accounts provided by witnesses (Zhao et al. 2021). The debris flow mass that rushed out of the gully blocked the river due to the local terrain constraints
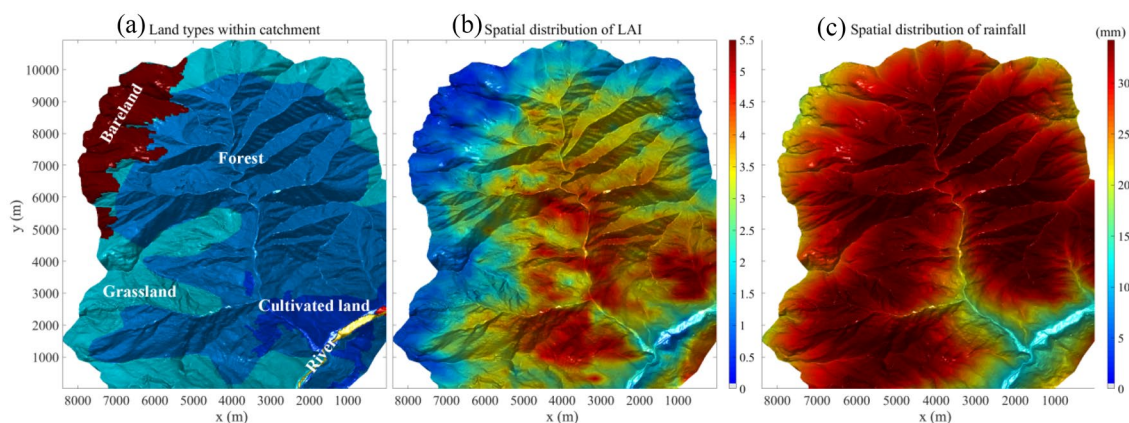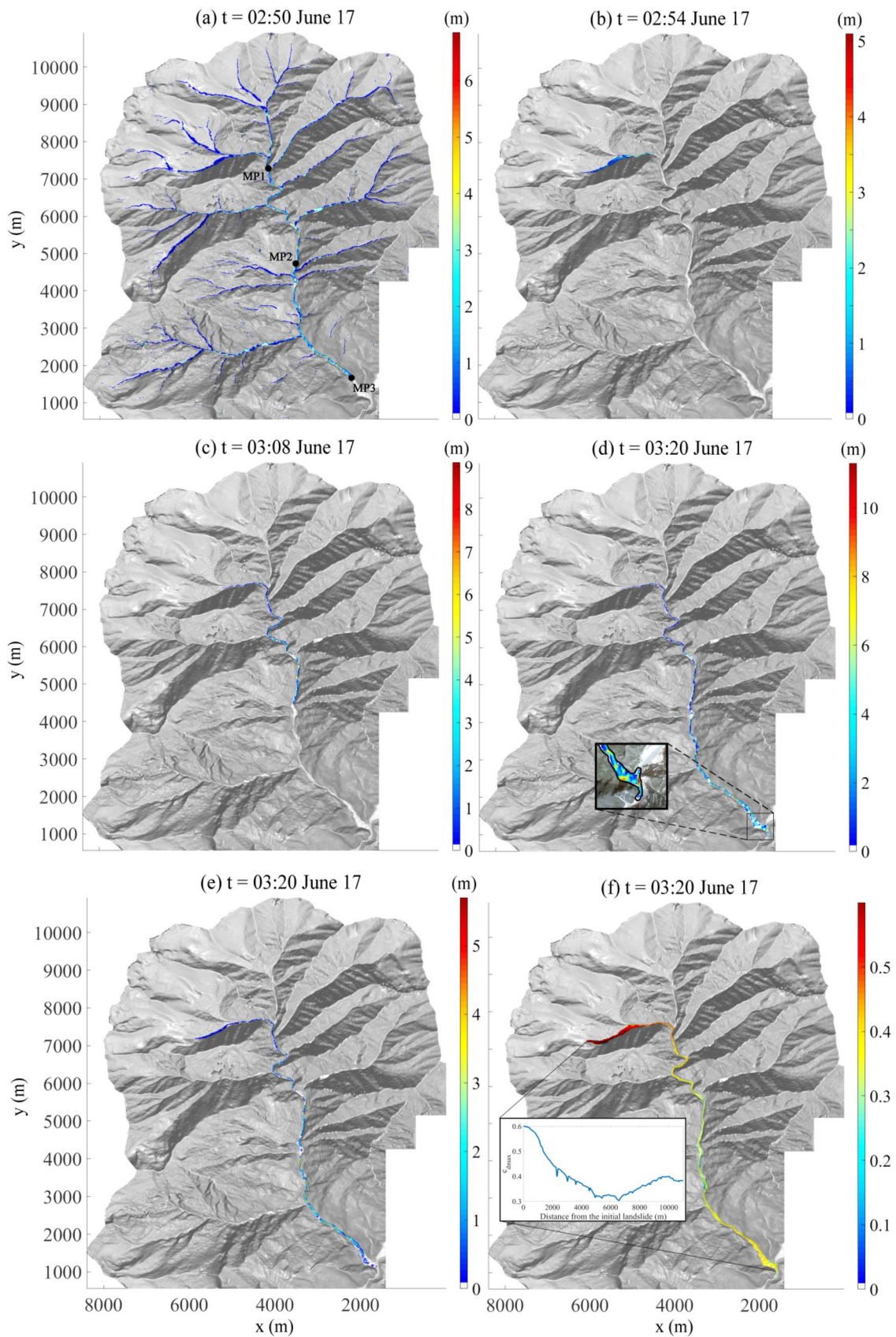

Fig. 5 a Land types within Meilong catchment include forest, grassland, cultivated land, and bareland and **b** the corresponding spatial distribution of *LAI*; **c** the spatial distribution of rainfall within Meilong catchment when its intensity located in the gully entrance equals to 11.4 mm/h

(a) t = 02:50 June 17

(b) t = 02:54 June 17

(c) t = 03:08 June 17

(d) t = 03:20 June 17

(e) t = 03:20 June 17

(f) t = 03:20 June 17

Fig. 6 Simulation results of **a** runoff pattern in catchment before shallow landslide collapsed, **b–d** debris flow patterns during the rainstorm from 02:50 to 03:20 June 17, and the deposition pattern of debris flow is shown in the subfigures in **d**; distributions of the erosion depth and the maximum solid volume concentration along debris flow path are shown in **e** and **f**, respectively. The maximum solid volume concentration (c_{dmax}) versus distance from the initial landslide along the center line of flow path is shown in the subfigures in **f**. Three monitoring points (MP1-3) in **a** are marked by black dot

(e.g. the elevated opposite river bank and reduced slope), forming a dam with a maximum height of 11.3 m which is consistent with the observed heights ranging from 8 to 12 m (Zhao et al. 2021). The calculated deposit area of the debris mass, depicted in Fig. 6d, also corresponds to the observed area. Approximately 3.36×10^5 m³ of sediment materials within the gully were eroded, with a significant portion originating from the lower section of the gully, where the scale and mobility of the debris flow were noticeably intensified. The erosion depths in the lower gully exhibit a range of 0.5 to 5.7 m, with an average depth of 3.2 m that is slightly lower than the value of 3.7 m reported by An et al. (2022) (see Fig. 6e). Figure 6f displays the maximum solid volume concentration observed in the debris flow path. It can be found that the solid volume concentration decreases firstly due to the mixing of runoff with the debris flow during propagation. The subsequent increase in solid volume concentration is caused by the intense erosion at the lower part of the gully and the escape of water from the deposited debris at the accumulation area. The results derived from the models exhibit agreement with existing data, including the timing of debris flow reaching the gully outlet, the maximum height of the debris dam, and the extent of the debris mass deposit area.

Figure 7a displays the flow discharges at three monitoring points in the catchment, providing insights into the variations. Meanwhile, Fig. 7b depicts the computation of scalar metrics, enabling a comprehensive interpretation of the numerical results concerning the energy of the debris flow. The graph in Fig. 7a shows a minimal change in debris flow discharge between monitoring points MP1 and MP2 but a significant increase between MP2 and MP3. This difference can be attributed to the low mobility of the debris mass in the upper part of the main gully, caused by the high solid volume concentration and a tortuous flow path. These factors limit the flow and contribute to the observed discrepancy. During this stage, the beneficial effect of erosion on debris flow propagation is minimal, primarily due to its small scale (Fig. 7b). Then, water absorption plays a critical role in the early stages of debris flow propagation by decreasing the basal shear stress of the debris mass and providing additional energy to the debris mass. The graph in Fig. 7a also clearly shows a noticeable decrease in the discharge of the runoff as the debris flow passes through. After the debris flow has passed the monitoring points, the discharge of runoff at these monitoring points tends to return to normal, due to the cessation of water absorption by the debris flow and the resumption of regular flow conditions in the catchment. Once the debris mass enters the lower portion of the main gully, the mobility of the debris flow is enhanced due to the favorable terrain conditions (e.g., relatively straight in channel profile and high in longitudinal gradient). Thus the sediment entrainment caused by the debris flow primarily occurs in the lower part of the gully, as indicated in

Fig. 6e. During this stage, the beneficial effect of erosion on debris flow propagation becomes appreciable compared to the effect from water absorption (Fig. 7b). We also calculate the case without considering water absorption. The results indicate that the kinetic energy of the debris mass decreases rapidly, resulting in a reduced erosion volume (see Fig. 7b). Understanding these dynamics helps to better comprehend the interplay between water absorption and erosion in the overall behavior of debris flows. These results also provide confidence in the feasibility of this method for future studies and evaluations related to debris flow dynamics and management strategies.

Significant variations in debris flow propagation are predicted by alternative simulations using the same rainfall condition but different values of E_m. As mentioned above, no accurate formulas exist for quantitative describe E_m, since the mixing process between water and viscosity flow is too complex. Considering the findings of Talling et al. (2002) and the assumption made in this scenario, three alternative values for E_m are proposed: $E_m = 0.001$, 0.01, and 1 m/min. These values reflect different flow properties (e.g., material and viscosity from weak to strong) of the debris flow. These variations have a considerable effect on the predicted runout distance of debris flows (see Fig. 8). The numerical results at 03:18 on June 17 provide a suitable basis for comparing the runout distance. This is because, in the simulation with an E_m value of 0.1 m/min, the debris flow reached the gully entrance at this specific time. Comparatively, smaller values of E_m are associated with shorter runout distances, while larger values of E_m are associated with longer runout distances. But the difference between the cases with $E_m = 0.001$ and 0.01 m/min is small. This may be due to the small value of E_m indicating a high viscosity of debris flow, making it hard to absorb water from runoff, finally leading to a small variation in the solid volume fraction of the debris flow and hence, the mobility. In the case with a larger value of E_m, the viscosity of debris flow may be small, and then solid-fluid segregation is easier to occur in debris flow propagation (e.g., dry debris flow front), which enhances the ability of debris mass to absorb runoff and thus increases the mobility. However, the case with $E_m = 1$ m/min has a large erosion depth (with a maximum depth of 11.2 m and an average depth of 5.5 m in the lower part of the main gully), which is far from the observed data (~ 3.2 m) (see Fig. 8e, f). It also should be noted that there is a significant difference in the runout distance of debris flow between the cases with $E_m = 0.01$ and 0.1 m/min, and the runout distance of the former case is only about one-half of the runout distance of the latter case. This significant difference may be caused by the combined effects of water absorption and terrain features. On the one hand, water absorption enhances the mobility and volume of debris flow, and this influence increases with the increase of E_m. On the other hand, local terrain variation (e.g., concave terrain) causes debris mass to accumulate until the volume of debris flow exceeds the storage (see Fig. 8a, b). For the case with $E_m = 0.01$ m/min, most of the materials in debris flow are intercepted by the concave terrain and thus the propagation of debris flow is slowed. By contrast, under the effects of water absorption and sediment entrainment, the volume of debris flow in the case with $E_m = 0.1$ m/min is large enough and only a part of the materials is intercepted when crossing this concave terrain.

According to Guo et al. (2021), elevation was identified as the dominant factor influencing rainfall variation, owing to intricate
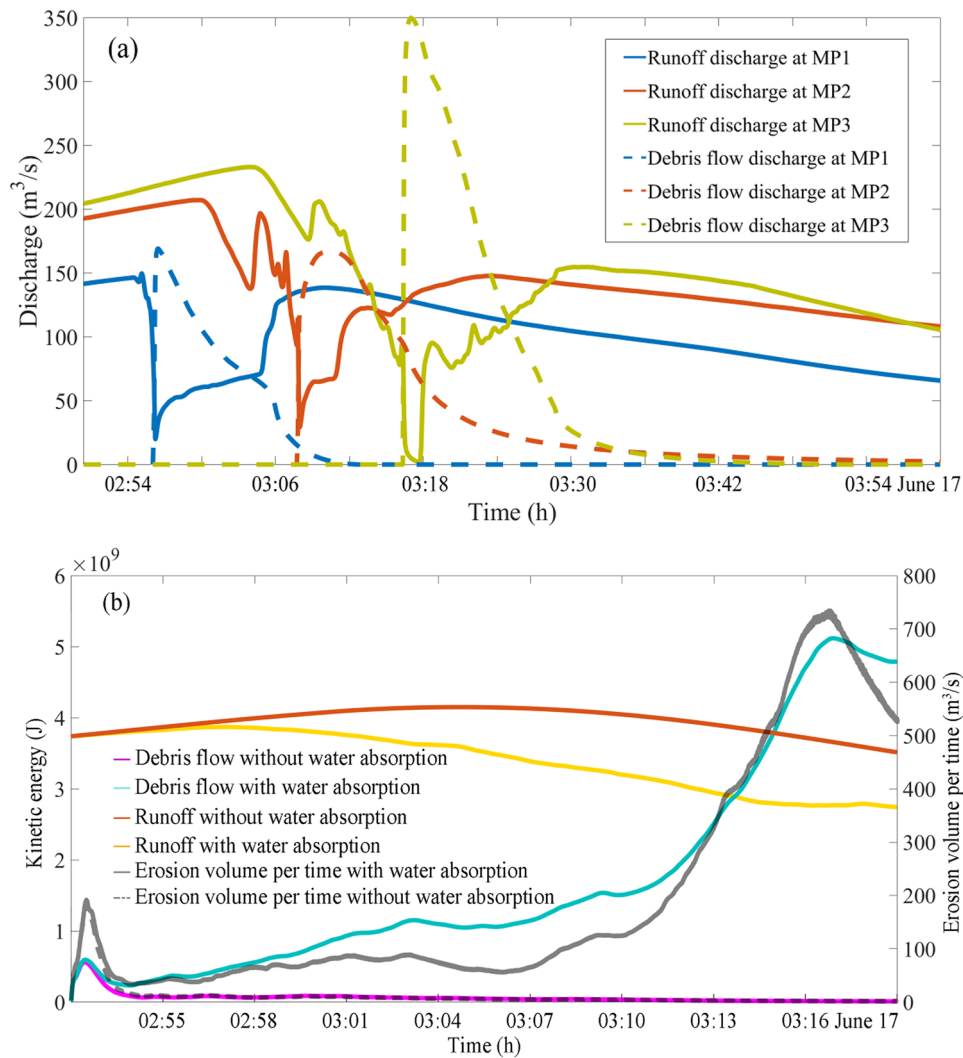
Fig. 7 **a** Discharges of debris flow and runoff at three monitoring points after the occurrence of landslide and **b** evolution of total kinetic energy (left) and erosion volume per time (right) in alternative Meilong debris flow simulations that employ two conditions of with and without water absorption

orographic conditions. For the Meilong catchment, which spans a substantial area of 62.55 km² and encompasses a significant elevation difference of 2708 m, this effect may potentially be more pronounced. Thus, different simulations with varying spatial rainfall distributions were conducted to assess their impact on runoff scaling. Clear trends emerge when scalar indices of debris flow mobility are calculated from the results of alternative simulations, which utilize a range of H values ranging from 2200 to 4600 m and E_m values ranging from 0.001 to 0.1 m/min. One index used to gauge the efficiency of debris flow energy conversion is obtained by dividing the peak kinetic energy (KED_{max}) by the peak total kinetic energy (KED_{tmax}) of all simulations that share the same value of E_m. A graph depicting the relationship between KED_{max}/KED_{tmax} and H and E_m (see Fig. 9a) reveals that, when E_m has a small value of 0.01 m/min, variations in H have a negligible effect on debris flow mobility. This is due to the limited translation of mass and energy from runoff into debris flow. In contrast, the mobility of the debris flow exhibits a more rapid increase with

larger values of E_m and H. These differences in debris flow mobility resulting from variations in H and E_m also lead to distinct trends in the ratio between the peak kinetic energy (KED_{max}) of the debris flow and the peak kinetic energy (KER_{max}) of the runoff (Fig. 9b). However, it is worth noting that the rate of increase in KED_{max}/KED_{tmax} slows down when H exceeds 3400 m when E_m is set to 0.1 m/min. It can be attributed to the fact that water absorption decreases the solid volume fraction of the debris mass, thereby reducing its erosion ability, despite enhancing overall debris flow mobility. Interestingly, this trend is not observed in the case where E_m is set to 1 m/min. It can be considered that the mass and velocity of the debris flow experience a substantial increase due to the mixing with runoff. As a result, sufficient sediment materials are eroded by the debris flow, thereby maintaining its solid volume fraction at a high level (Fig. 9c). Moreover, with a small value of E_m, the debris flow is unable to acquire sufficient energy and mass to overcome the local concave terrain mentioned earlier, and thus the value of KED_{max}/KER_{max} decreases as
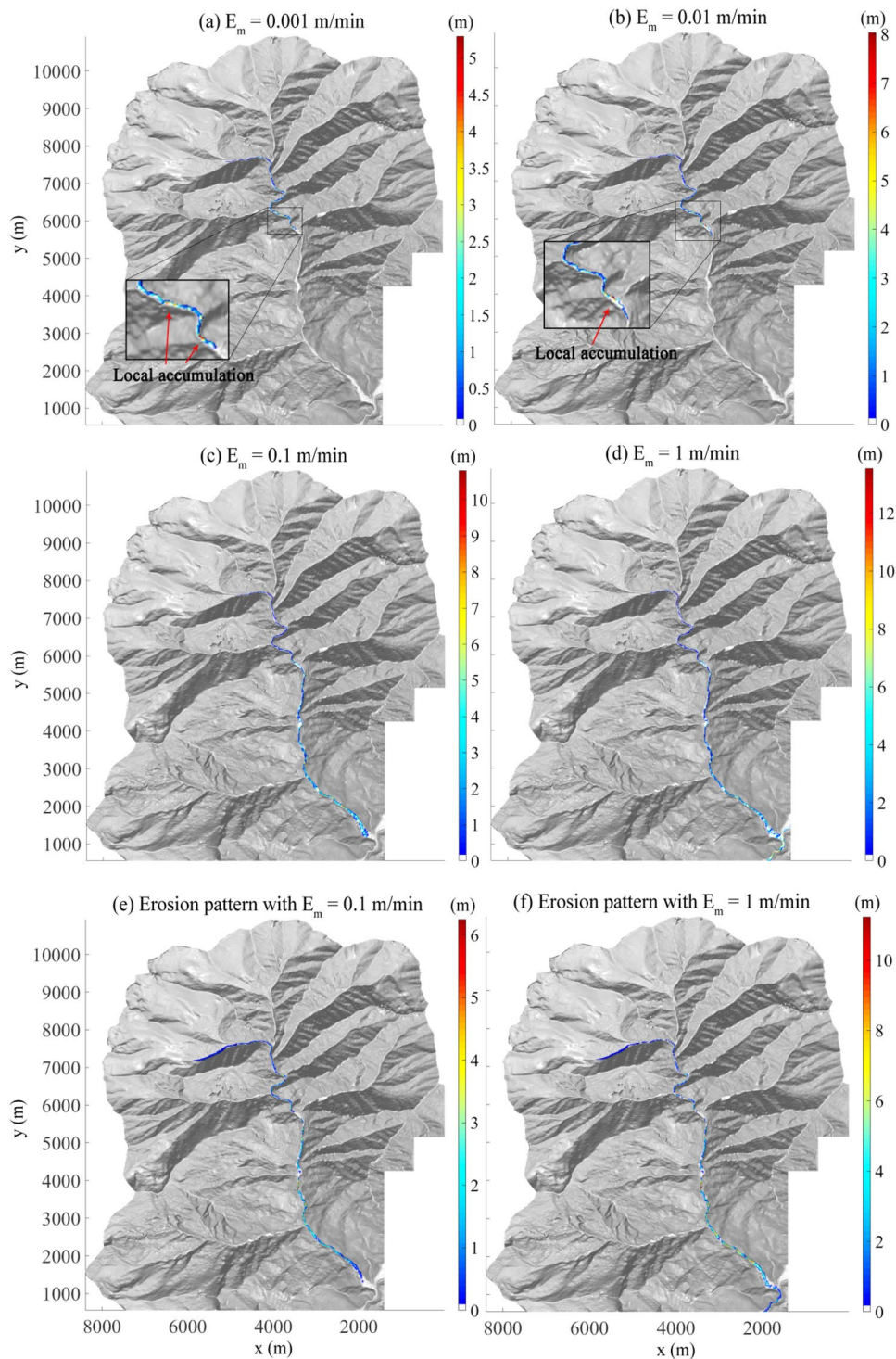
Fig. 8 a–d Propagation distance of debris flow at 03:18 June 17 in alternative Meilong debris flow simulations that employ different values of E_m from 0.001 to 1 m/min; the corresponding erosion patterns with **e** $E_m = 0.1$ m/min and **f** $E_m = 1$ m/min

H increases (Fig. 9b). In other cases with larger values of E_m, the debris flow successfully traverses the concave terrain and enters the lower portion of the main gully when $H > 2600$ m (indicated by the gray line in Fig. 9b). More sediment is eroded by the debris flow to augment its energy, and thus the value of KED_{max}/KER_{max} increases. However, as H increases, the rate of increase in KER_{max} is greater than that of KED_{max}, resulting in a decrease in the value of KED_{max}/KER_{max}.
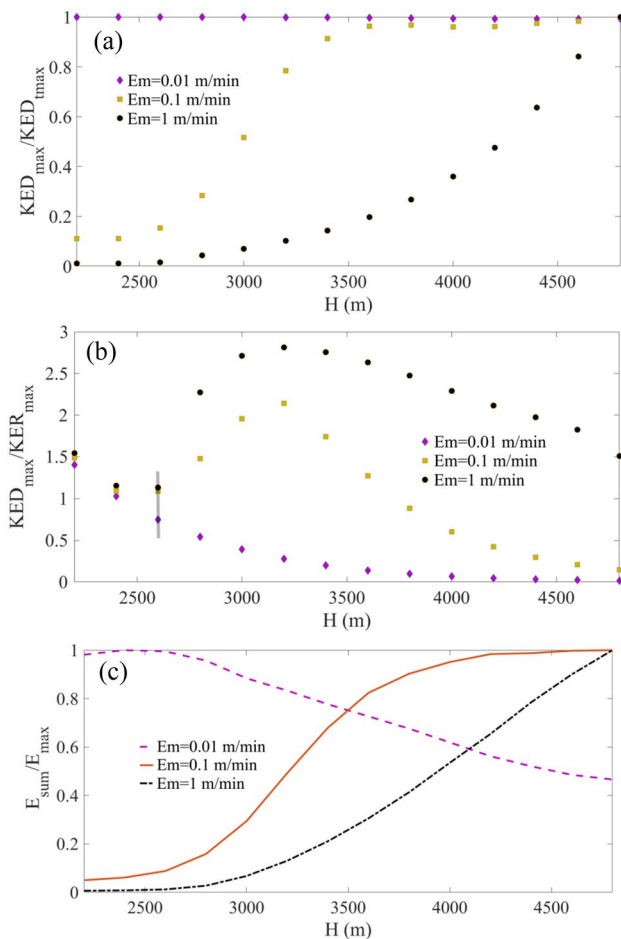
Fig. 9 Indexes for reflecting the effects of water absorption rate and H on debris flow mobility, including **a** KED_{max}/KED_{tmax}, **b** KED_{max}/KER_{max}, and **c** E_{sum}/E_{tmax}, because water absorption determines the amount of mass and momentum transferred from runoff to debris flow and thereby influences kinetic energy of debris flow and runoff. E_{sum} and E_{tmax} refer to the total volume of eroded sediments and the peak total volume of eroded sediments of all simulations with the same value of E_m

Discussion

Rainfall intermittency and debris flow propagation

All the simulations conducted thus far utilized the same fundamental rainfall data, which was obtained from the Banshanmen meteorological station located 3 km away from the Meilong catchment. It is important to note that this rainfall data has a significant influence on the dynamics of runoff and, consequently, the propagation of debris flow. While studies have examined the impact of rainfall intermittency on slope failure (von Ruette et al. 2014), its specific effect on debris flow propagation remains unclear. To investigate the sensitivity of debris flow propagation to rainfall intermittency, simulations were conducted for rainfall with a total amount of 34.4 mm but with varying time distributions between 22:00 on June 16 and 03:20 on June 17 as illustrated in Fig. 10. It is evident that rainfall intermittency has a significant impact on

debris flow propagation, particularly when considering water absorption. This is attributed to the discontinuity in rainfall, which results in a reduction in runoff discharge. The discontinuous nature of rainfall during debris flow events hinders the accumulation of sufficient mass and energy from runoff, particularly during its initial stages. As a result, the propagation velocity of the debris flow is delayed. This delay becomes more pronounced with longer periods of discontinuous rainfall.

In the case with larger value of E_m, this delayed effect is enlarged because debris flow can absorb more runoff mass under the same condition of runoff, while rainfall intermittency will cause more loss in runoff discharge. It is important to acknowledge that our study solely focuses on examining the impact of rainfall intermittency on debris flow mobility, without considering its effect on slope failure. However, it is worth noting that rainfall intermittency can influence both of these factors, and the relationship between them is complex. Further investigation is required to fully understand and analyze the interplay between rainfall intermittency, slope failure, and debris flow mobility, warranting future research endeavors.

Catchment characteristics and debris flow mobility

The results depicted in Fig. 7b provide valuable insights into the influence of water absorption on the propagation of debris flow. This perspective offers a novel explanation for the relationship between the susceptibility of debris flow and rainfall that triggers runoff. The analysis of data collected from 78 debris flow events, as documented in previous studies (Huang and Tang 2014; Tang et al. 2012a, b), reveals that both the catchment area (A) and catchment internal relief (H) have a notable influence on the length of deposit (L_f), as illustrated in Fig. 11. As the values of A and H increase, L_f for debris flow events also tends to increase. In general, when the values of A and H are relatively small, debris flows are more likely to exhibit smaller L_f values. From the perspective of water absorption, it can be argued that in a catchment with larger values of A and H, it is more favorable to generate runoff with large discharge under the same rainfall conditions, which satisfies $E_m < h_1$ and thus provides enough mass and momentum from runoff into debris flows through the mixture and enhances debris flow mobility. In contrast, the generated runoff in a small catchment has a small discharge and may not be able to meet the absorption capacity of debris flow (e.g., $E_m > h_1$), and thus provides less mass and momentum to debris flow (Fig. 12). This accelerated transfer leads to an increased propagation velocity and subsequently, a larger value of L_f for debris flow events. Thus, catchments with larger values of A and H are more prone to experiencing debris flows with larger extents. This effect is particularly sensitive for debris flow cases that involve a small volume of initial mass. In such instances, the transfer of mass and energy from runoff into debris flows through a mixture, facilitated by larger values of A and H, has a more pronounced impact on the propagation velocity and the resulting extent of the debris flow. Indeed, the runout distance of a debris flow is influenced by numerous factors, including the initiation position and local terrain of the channel. While L_f is used as an indicator of debris flow mobility, it does not entirely capture the complexity of debris flow movement as it is constrained by the local terrain at the gully entrance. Nevertheless, the water absorption from runoff to debris flow provides a
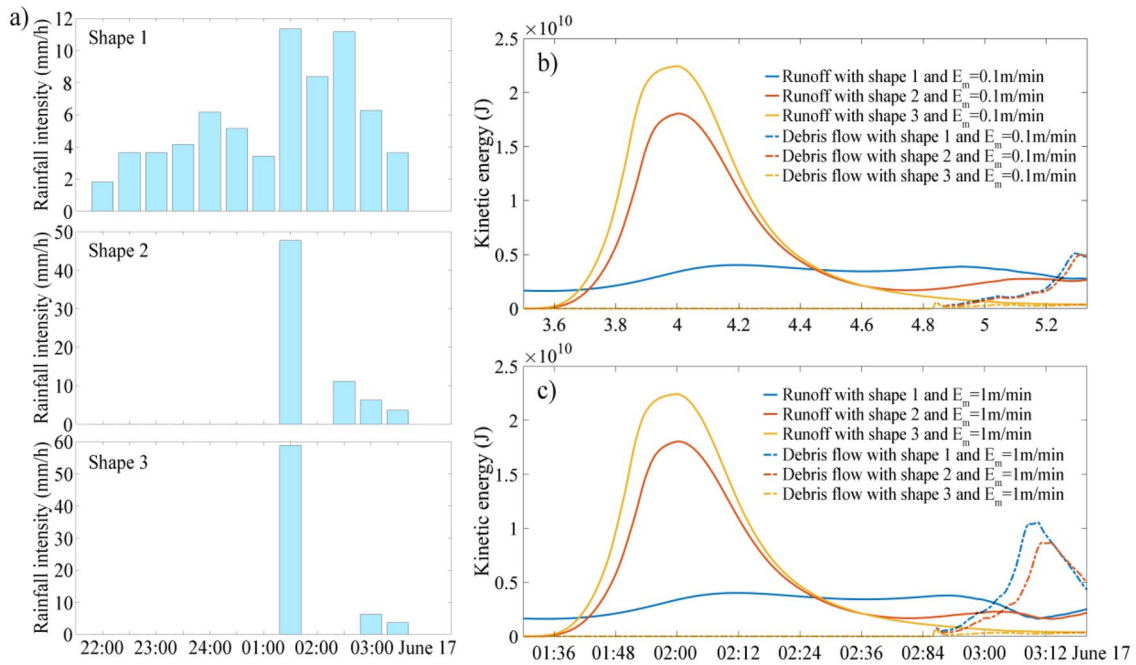
Fig. 10 Analysis of debris flow propagation under the effect of rainfall intermittency by considering three rainfall shapes (**a**), and the corresponding evolutions of the kinetic energy for runoff and debris flow are shown in **b** with $E_m = 0.1$ m/min and **c** with $E_m = 1$ m/min

fresh perspective to explain why debris flows trend to have longer runout distances in larger basins. However, further calibration of this relationship requires additional standardized field data.

Fig. 11 Correlations for **a** catchment area A and maximum runout distance L_f, and for **b** catchment internal relief H and maximum runout distance L_f, based on the existing data from (**a**) Tang et al. (2012a), (**b**) Tang et al. (2012b) and (**c**) Huang and Tang (2014). The gray line represents the trend between these variables

Limitation of the simulations

The limitation of these simulations mainly lies in the available verification data, the quality of the dataset, and the mechanisms involved in the applied physical model. Firstly, the absence of field monitoring data hinders the calibration of the presented model. Only limited field data were applied here, such as averaged erosion depth and deposition area. Actual rainfall data, runoff flux, and debris flow velocity are challenging to obtain through remote sensing and field observations post-event. It is crucial to prioritize long-term systematic monitoring in a catchment to address these limitations. Secondly, the dataset used in this study comprises
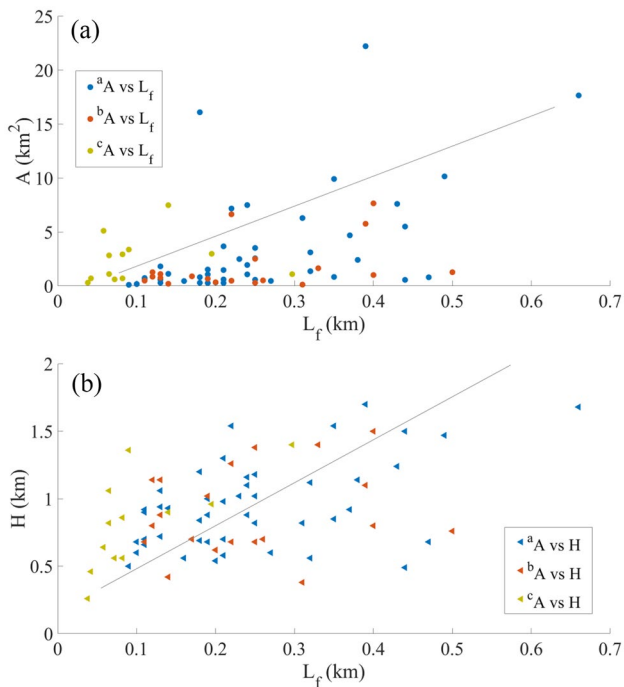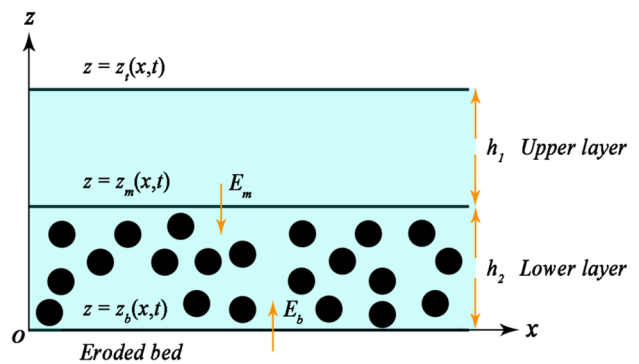

Fig. 12 A simple schematic diagram of a shallow water layer on top of the debris flow layer, in turn flowing over an eroded bed. h_1 and h_2 are the thicknesses of the upper and lower layers, respectively; z_t, z_m, and z_b represent the free surface between the upper layer and air, the middle interface between two layers, and the bottom surface between the lower layer and bed. E_m and E_b represent the mass transfer across the boundaries z_m and z_b, respectively

rainfall intensity, terrain data, and *LAI*. Due to the significance of vegetation interception processes, the qualities of rainfall intensity and *LAI* play a pivotal role in calculating the effective precipitation that contributes to runoff. However, the resolutions of these datasets are not uniform, and finer-scale data is currently unavailable. The development of a high-precision and high-resolution dataset would be instrumental in enhancing the accuracy of simulation results and improving overall model performance. Thirdly, despite the establishment of a corresponding general framework, there is still a lack of investigation into the physical mechanisms involved. This limitation hinders a comprehensive understanding of debris flow propagation. The current model offers limited advantages in terms of physical mechanics when compared to the available data, particularly in relation to water absorption, which plays a crucial role in debris flow propagation. Further research and development are needed to enhance the understanding and integration of physical mechanics into the model, ultimately improving its predictive capabilities. Fourthly, the deposition and restart processes of debris mass during its propagation are influenced by various factors, including grain size, fluid viscosity, and flow velocity. These factors exhibit temporal variation, leading to dynamic changes in their values within the model. However, due to unclear mechanisms associated with these changes, the current study employs constant and uniform values for the model parameters. This limitation highlights the need for further investigation and understanding of the temporal dynamics of these factors in order to improve parameterization within the model.

Conclusion

In this study, we proposed a numerical framework to evaluate the effect of water absorption on debris flow propagation, and the 2020 Meilong debris flow event was simulated and analyzed as an example. This numerical framework consists of two parts. The first is a coupled model that considers rainfall spatial distribution, vegetation interception, and soil infiltration, which calculates the effective precipitation contributed to runoff. To consider the spatial feature of rainfall, an elevation-based formula was adopted. The second is a depth-averaged two-layer model that considers the interaction between runoff and debris mass by introducing a new parameter of water absorption, which calculates the dynamic features (depth and velocity) of runoff and debris flow. Due to an unclear mechanism of water absorption between runoff and debris mass, certain constant values of water absorption rate were used for simplicity. The process of the 2020 Meilong debris flow event was simulated first, and the results were found to be consistent with those obtained from field investigation and other simulation results. For this debris flow event, water absorption played a key role in the early stage of debris flow propagation by decreasing the basal shear stress and supplying additional energy to the debris mass. Alternative simulations with different values of H and E_m were performed to study the influence of these key factors on debris flow propagation. Both indicate that strong runoff dynamics enhances the mobility of debris flow. Furthermore, the results show that rainfall intermittency can alter the propagation velocity of debris flow by changing runoff dynamics. Available field data of debris flow event shows that debris flow mobility increases with the increase of catchment area, due to the

dynamics of runoff in larger catchment areas prone to becoming strong, thus influencing debris flow propagation through water absorption. It may offer a novel perspective to explain the correlation between rainfall intensity and debris flow susceptibility on the catchment scale.

Data availability

All data used in this work are either publicly available or available from the authors upon reasonable request.

Declarations

Competing interests The authors declare no competing interests.

Appendix. Derivation of the two-layer model by considering mass transfer at intermediate interface

Basic equations

The fundamental laws for mass and momentum conservations for an incompressible continuum are expressed as follows:

$$\left.\begin{array}{l} \partial_t \gamma_m + \nabla \cdot \left(\gamma_m \mathbf{U}_m \right) = 0 \\ \partial_t \left(\gamma_m \mathbf{U}_m \right) + \nabla \cdot \left(\gamma_m \mathbf{U}_m \otimes \mathbf{U}_m \right) = -\nabla \cdot \mathbf{T}_m \end{array}\right\} \tag{13}$$

where $\mathbf{U}_m = (u_{1,2}, v_{1,2}, w_{1,2})$ is the medium velocity field, in which the subscript $m = (1, 2)$ refers to the upper layer and lower layer, respectively; γ_m is the medium density keeping constant; t is time; and $\mathbf{T}_m$ is the Cauchy stress tensor.

Boundary kinematic conditions

To express the boundary variation, such as the rates of boundary elevation change and the rates of material flux through each boundary, kinematic and dynamic boundary conditions are applied at the top and bottom boundary of any layer.

Kinematic boundary conditions imposed at the top and bottom interface of the upper layer are expressed as follows:

$$z_m(x, t) = z_t(x, t) - h_1 = 0 \tag{14}$$

$$
\left.
\begin{array}{l}
w_1(z_t) = \frac{\partial z_t}{\partial t} + u_1(z_t)\frac{\partial z_t}{\partial x} + v_1(z_t)\frac{\partial z_t}{\partial y} \\
w_1(z_m) = \frac{\partial z_m}{\partial t} + u_1(z_m)\frac{\partial z_m}{\partial x} + v_1(z_m)\frac{\partial z_m}{\partial y} - E_m
\end{array}
\right\}
\tag{15}
$$

where E_m is the mixture rate from runoff to debris flow as volumetric fluxes per unit boundary area normal to the bottom boundary z_m.

Kinematic boundary conditions imposed at the top and bottom interface of the lower layer are expressed as follows:

$$
z_b(x,t) = z_t(x,t) - h_1 - h_2 = 0
\tag{16}
$$

$$
\left.
\begin{array}{l}
w_2(z_m) = \frac{\partial z_m}{\partial t} + u_2(z_m)\frac{\partial z_m}{\partial x} + v_2(z_m)\frac{\partial z_m}{\partial y} - E_m \\
w_2(z_b) = \frac{\partial z_b}{\partial t} + u_2(z_b)\frac{\partial z_b}{\partial x} + v_2(z_b)\frac{\partial z_b}{\partial y} + E_b
\end{array}
\right\}
\tag{17}
$$

where E_b is entrainment rate of sediments as volumetric fluxes per unit boundary area normal to the bottom boundary.

The free surface of the two-layer is stress-free condition:

$$
\mathbf{T}_m \cdot \mathbf{n} = 0
\tag{18}
$$

$$
\int_{z_m}^{z_t}(LHS)dz \int_{z_m}^{z_t}\left[\frac{\partial}{\partial t}(\gamma_1 u_1) + \frac{\partial}{\partial x}(\gamma_1 u_1^2) + \frac{\partial}{\partial y}(\gamma_1 u_1 v_1) + \frac{\partial}{\partial z}(\gamma_1 u_1 w_1)\right]dz = \frac{\partial}{\partial t}(\gamma_1 h_1 \overline{u}_1) + \frac{\partial}{\partial x}\left(\gamma_1 h_1 \overline{u}_1^2\right) + \frac{\partial}{\partial y}(\gamma_1 h_1 \overline{uv}_1)
$$
$$
+ \gamma_1(z_t)u_1(z_t)\left[w_1(z_t) - \frac{\partial z_t}{\partial t} - u_1(z_t)\frac{\partial z_t}{\partial x} - v_1(z_t)\frac{\partial z_t}{\partial y}\right]
$$
$$
- \gamma_1(z_m)u_1(z_m)\left[w_1(z_m) - \frac{\partial z_m}{\partial t} - u_1(z_m)\frac{\partial z_m}{\partial x} - v_1(z_m)\frac{\partial z_m}{\partial y}\right]
\tag{23}
$$

where $\mathbf{n}$ is the exterior unit normal vector. Dynamic boundary conditions for the upper and lower layers are assumed to satisfy Manning friction law and combined friction law that couples Coulomb friction law and Manning friction law, respectively.

$$
\left.
\begin{array}{l}
\mathbf{pn} - \mathbf{n}(\mathbf{n}\cdot\mathbf{pn}) = -\gamma_1\mathbf{g}n_b(\mathbf{u}_1 - \mathbf{u}_2)|\mathbf{u}_1 - \mathbf{u}_2|/h_1^{4/3} \\
\mathbf{pn} - \mathbf{n}(\mathbf{n}\cdot\mathbf{pn}) = -\left[(\mathbf{u}_2/|\mathbf{u}_2|)c_d\tan\varphi_{bed}(\mathbf{n}\cdot\mathbf{pn}) + (1-c_d)\gamma_2\,\mathbf{g}n_b\mathbf{u}_2|\mathbf{u}_2|/h_2^{4/3}\right]
\end{array}
\right\}
\tag{19}
$$

where $\mathbf{pn}$, $\mathbf{n}\cdot\mathbf{pn}$ and $\mathbf{pn}-\mathbf{n}(\mathbf{n}\cdot\mathbf{pn})$ represent the negative traction vector, normal pressure, and negative shear traction, respectively; $\mathbf{g} = (g_x, g_y, g_z)$ is the gravity components.

Depth-integrated equations for upper layer

Before driving the equations by integration, some mean values are defined as follows:

$$
\overline{u} = \frac{1}{h}\int_{z_1}^{z_2}udz; \ \overline{v} = \frac{1}{h}\int_{z_1}^{z_2}vdz; \ \overline{w} = \frac{1}{h}\int_{z_1}^{z_2}wdz; \ \overline{\tau} = \frac{1}{h}\int_{z_1}^{z_2}\tau dz
\tag{20}
$$

where z_1 and z_2 refer to the top-bottom boundaries of any layer with a thickness h and a stress tensor τ. The superscript "–" refers to the depth-averaged form of any value.

Using Leibniz's formula to integrate the mass balance equation of the upper layer

$$
\int_{z_m}^{z_t}\left[\frac{\partial \gamma_1}{\partial t} + \frac{\partial}{\partial x}(\gamma_1 u_1) + \frac{\partial}{\partial y}(\gamma_1 v_1) + \frac{\partial}{\partial z}(\gamma_1 w_1)\right]dz = \frac{\partial}{\partial t}\int_{z_m}^{z_t}\gamma_1 dz - \gamma_1(z_t)\frac{\partial z_t}{\partial x} + \gamma_1(z_m)\frac{\partial z_m}{\partial x}
$$
$$
+ \frac{\partial}{\partial x}\int_{z_m}^{z_t}(\gamma_1 u_1)dz - \gamma_1(z_t)u_1(z_t)\frac{\partial z_t}{\partial x} + \gamma_1(z_m)u_1(z_m)\frac{\partial z_m}{\partial x}
$$
$$
+ \frac{\partial}{\partial y}\int_{z_m}^{z_t}(\gamma_1 v_1)dz - \gamma_1(z_t)v_1(z_t)\frac{\partial z_t}{\partial y} + \gamma_1(z_m)v_1(z_m)\frac{\partial z_m}{\partial y}
$$
$$
+ \gamma_1(z_t)w_1(z_t) - \gamma_1(z_m)w_1(z_m)
\tag{21}
$$

We assume that $\partial h_1/\partial t = \partial z_t/\partial t - \partial z_m/\partial t$ and then couple Eqs. (15) and (21) to obtain

$$
\frac{\partial}{\partial t}(\gamma_1 h_1) + \frac{\partial}{\partial x}(\gamma_1 h_1 \overline{u}_1) + \frac{\partial}{\partial y}(\gamma_1 h_1 \overline{v}_1) = -\gamma_1(z_m)E_m
\tag{22}
$$

Take the momentum equation in x direction as an example, its left-hand side is changed into

By coupling Eqs. (15) and (23) to obtain

$$
\int_{z_m}^{z_t}(LHS)dz = \frac{\partial}{\partial t}(\gamma_1 h_1 \overline{u}_1) + \frac{\partial}{\partial x}\left(\gamma_1 h_1 \overline{u}_1^2\right) + \frac{\partial}{\partial y}(\gamma_1 h_1 \overline{u}_1 \overline{v}_1) + \gamma_1(z_m)u_1(z_m)E_m
\tag{24}
$$

The right-hand side of the x-momentum equation for the upper layer yields

$$
\int_{z_m}^{z_t}(RHS)dz = \int_{z_m}^{z_t}-\left(\frac{\partial\tau_{xx}}{\partial x} + \frac{\partial\tau_{xy}}{\partial y} + \frac{\partial\tau_{xz}}{\partial z}\right)dz
$$
$$
= -\frac{\partial}{\partial x}(h_1\overline{\tau}_{xx}) - \frac{\partial}{\partial y}(h_1\overline{\tau}_{xy}) + \tau_{xx}(z_t)\frac{\partial z_t}{\partial x} - \tau_{xx}(z_m)\frac{\partial z_m}{\partial x} + \tau_{xy}(z_t)\frac{\partial z_t}{\partial y} - \tau_{xy}(z_m)\frac{\partial z_m}{\partial y} - \tau_{xz}(z_t) + \tau_{xz}(z_m)
\tag{25}
$$

Based on Eq. (18), kinematic and stress condition at the free surfaces are as follows:

$$
\left.
\begin{array}{l}
\tau_{xy}(z_t) = \tau_{xx}(z_t) = \tau_{xz}(z_t) = \tau_{xy}(z_m) = 0 \\
\overline{\tau}_{xx} = \frac{1}{2}\left[\tau_{xx}(z_t) + \tau_{xx}(z_m)\right] = \frac{1}{2}\gamma_1 g h_1
\end{array}
\right\}
\tag{26}
$$

With Eq. (26), the right-hand side of the x-momentum equation is changed into

$$
\int_{z_m}^{z_t}(RHS)dz = -\frac{\partial}{\partial x}\left(\frac{1}{2}\gamma_1 g h_1^2\right) - \gamma_1 g h_1 \frac{\partial z_m}{\partial x} + \tau_{xz}(z_m)
\tag{27}
$$

Thus, we obtain the depth-averaged x-momentum equation of the upper layer as

$$\frac{\partial}{\partial t}\left(\gamma_1 h_1 \bar{u}_1\right) + \frac{\partial}{\partial x}\left(\gamma_1 h_1 \bar{u}_1^2 + \frac{1}{2}\gamma_1 g h_1^2\right) + \frac{\partial}{\partial y}\left(\gamma_1 h_1 \bar{u}_1 \bar{v}_1\right) = -\gamma_1\left(z_m\right)u_1\left(z_m\right)E_m$$

$$-\gamma_1 g h_1 \frac{\partial z_m}{\partial x} - \frac{\gamma_1 g_z n_b}{h_1^{1/3}}\left(\bar{u}_1 - \bar{u}_2\right)\left|\bar{\mathbf{u}}_1 - \bar{\mathbf{u}}_2\right|$$

$$(28)$$

Using similar procedure, the depth-averaged y-momentum component for the upper layer is obtained

$$\frac{\partial}{\partial t}\left(\gamma_1 h_1 \bar{v}_1\right) + \frac{\partial}{\partial x}\left(\gamma_1 h_1 \bar{u}_1 \bar{v}_1\right) + \frac{\partial}{\partial y}\left(\gamma_1 h_1 \bar{v}_1^2 + \frac{1}{2}\gamma_1 g h_1^2\right) = -\gamma_1\left(z_m\right)v_1\left(z_m\right)E_m$$

$$-\gamma_1 g h_1 \frac{\partial z_m}{\partial y} - \frac{\gamma_1 g_z n_b}{h_1^{1/3}}\left(\bar{v}_1 - \bar{v}_2\right)\left|\bar{\mathbf{u}}_1 - \bar{\mathbf{u}}_2\right|$$

$$(29)$$

Depth-integrated equations for lower layer

Also using the Leibnitz rule to interchange the mass balance equation of the lower layer

$$\int_{z_b}^{z_m}\left[\frac{\partial \gamma_2}{\partial t} + \frac{\partial}{\partial x}\left(\gamma_2 u_2\right) + \frac{\partial}{\partial y}\left(\gamma_2 v_2\right) + \frac{\partial}{\partial z}\left(\gamma_2 w_2\right)\right]dz = \frac{\partial}{\partial t}\int_{z_b}^{z_m}\gamma_2 dz - \gamma_2\left(z_m\right)\frac{\partial z_m}{\partial x} + \gamma_2\left(z_b\right)\frac{\partial z_b}{\partial x}$$

$$+ \frac{\partial}{\partial x}\int_{z_b}^{z_m}\left(\gamma_2 u_2\right)dz - \gamma_2\left(z_m\right)u_2\left(z_m\right)\frac{\partial z_m}{\partial x} + \gamma_2\left(z_b\right)u_2\left(z_b\right)\frac{\partial z_b}{\partial x}$$

$$+ \frac{\partial}{\partial y}\int_{z_b}^{z_m}\left(\gamma_2 v_2\right)dz - \gamma_2\left(z_m\right)v_2\left(z_m\right)\frac{\partial z_m}{\partial y} + \gamma_2\left(z_b\right)v_2\left(z_b\right)\frac{\partial z_b}{\partial y}$$

$$+ \gamma_2\left(z_m\right)w_2\left(z_m\right) - \gamma_2\left(z_b\right)w_2\left(z_b\right)$$

$$(30)$$

Coupling Eqs. (17) and (30) to obtain

$$\frac{\partial}{\partial t}\left(\gamma_2 h_2\right) + \frac{\partial}{\partial x}\left(\gamma_2 h_2 \bar{u}_2\right) + \frac{\partial}{\partial y}\left(\gamma_2 h_2 \bar{v}_2\right) = \gamma_2\left(z_m\right)E_m + \gamma_2\left(z_b\right)E_b \quad (31)$$

Integrating the momentum equation for this layer is similar with that of the upper layer. The left-hand side of the x-momentum equation of the lower layer is written as follows:

$$\int_{z_b}^{z_m}(LHS)dz = \int_{z_b}^{z_m}\left[\frac{\partial}{\partial t}\left(\gamma_2 u_2\right) + \frac{\partial}{\partial x}\left(\gamma_2 u_2^2\right) + \frac{\partial}{\partial y}\left(\gamma_2 u_2 v_2\right) + \frac{\partial}{\partial z}\left(\gamma_2 u_2 w_2\right)\right]dz = \frac{\partial}{\partial t}\left(\gamma_2 h_2 \bar{u}_2\right) + \frac{\partial}{\partial x}\left(\gamma_2 h_2 \bar{u}_2^2\right) + \frac{\partial}{\partial y}\left(\gamma_2 h_2 \bar{u}_2 \bar{v}_2\right)$$

$$+ \gamma_2\left(z_m\right)u_2\left(z_m\right)\left[w_2\left(z_m\right) - \frac{\partial z_m}{\partial t} - u_2\left(z_m\right)\frac{\partial z_m}{\partial x} - v_2\left(z_m\right)\frac{\partial z_m}{\partial y}\right]$$

$$- \gamma_2\left(z_b\right)u_2\left(z_b\right)\left[w_2\left(z_b\right) - \frac{\partial z_b}{\partial t} - u_2\left(z_b\right)\frac{\partial z_b}{\partial x} - v_2\left(z_b\right)\frac{\partial z_b}{\partial y}\right]$$

$$(32)$$

By applying the kinematic boundary conditions (Eq. 17), the left-hand side of the x-momentum equation of the lower layer is changed into

$$\int_{z_b}^{z_m}(LHS)dz = \frac{\partial}{\partial t}\left(\gamma_2 h_2 \bar{u}_2\right) + \frac{\partial}{\partial x}\left(\gamma_2 h_2 \bar{u}_2^2\right) + \frac{\partial}{\partial y}\left(\gamma_2 h_2 \bar{u}_2 \bar{v}_2\right)$$

$$- \gamma_2\left(z_m\right)u_1\left(z_m\right)E_m - \gamma_2\left(z_b\right)u_2\left(z_b\right)E_b$$

$$(33)$$

The right-hand side of the x-momentum equation for the lower layer yields

$$\int_{z_b}^{z_m}(RHS)dz = \int_{z_b}^{z_m} - \left(\frac{\partial \tau_{xx}}{\partial x} + \frac{\partial \tau_{xy}}{\partial y} + \frac{\partial \tau_{xz}}{\partial z}\right)dz$$

$$= -\frac{\partial}{\partial x}\left(h_2 \bar{\tau}_{xx}\right) + \frac{\partial}{\partial y}\left(h_2 \bar{\tau}_{xy}\right) + \tau_{xx}\left(z_m\right)\frac{\partial z_m}{\partial x} - \tau_{xx}\left(z_b\right)\frac{\partial z_b}{\partial x}$$

$$+ \tau_{xy}\left(z_m\right)\frac{\partial z_m}{\partial y} - \tau_{xy}\left(z_b\right)\frac{\partial z_b}{\partial y} - \tau_{xz}\left(z_m\right) + \tau_{xz}\left(z_b\right)$$

$$(34)$$

We assume that the normal stresses in the z direction are hydrostatic and thus

$$\tau_{zz}\left(z_b\right) = \gamma_1 g h_1 + \gamma_2 g h_2 \quad (35)$$

$$\bar{\tau}_{zz} = \frac{\tau_{zz}\left(z_m\right) + \tau_{zz}\left(z_b\right)}{2} = \frac{1}{2}\left(2\gamma_1 g h_1 + \gamma_2 g h_2\right) \quad (36)$$

The depth-averaged normal stresses are related to the normal stress based on the Mohr–Coulomb theory and so that

$$\bar{\tau}_{xx} = \bar{\tau}_{yy} = k_{ap}\bar{\tau}_{zz} = \frac{1}{2}k_{ap}\left(2\gamma_1 g h_1 + \gamma_2 g h_2\right) \quad (37)$$

where k_{ap} is the lateral stress coefficient. By neglecting the lateral shear stress terms in Eq. (34), the right side of the x-momentum equation for the lower layer is expressed as follows:

$$\int_{z_b}^{z_m}(RHS)dz = -\frac{\partial}{\partial x}\left[\frac{1}{2}k_{ap}\left(2\gamma_1 g h_1 h_2 + \gamma_2 g h_2^2\right)\right]$$

$$+ \gamma_1 g h_1 \frac{\partial z_m}{\partial x} - k_{ap}\left(\gamma_1 g h_1 + \gamma_2 g h_2\right)\frac{\partial z_b}{\partial x} - \tau_{xz}\left(z_m\right) + \tau_{xz}\left(z_m\right)$$

$$(38)$$

Thus, we obtain the depth-averaged x-momentum equation of the lower layer as follows:

$$\frac{\partial}{\partial t}\left(\gamma_2 h_2 \bar{u}_2\right) + \frac{\partial}{\partial x}\left(\gamma_2 h_2 \bar{u}_2^2 + \frac{1}{2}k_{ap}\gamma_2 g h_2^2 + k_{ap}\gamma_1 g h_1 h_2\right) + \frac{\partial}{\partial y}\left(\gamma_2 h_2 \bar{u}_2 \bar{v}_2\right) = \gamma_2\left(z_m\right)u_1\left(z_m\right)E_m + \gamma_2\left(z_b\right)u_2\left(z_b\right)E_b$$

$$+ \gamma_1 g h_1 \frac{\partial z_m}{\partial x} - k_{ap}\left(\gamma_1 g h_1 + \gamma_2 g h_2\right)\frac{\partial z_b}{\partial x} + \frac{\gamma_1 g_z n_b}{h_1^{1/3}}\left(\bar{u}_1 - \bar{u}_2\right)\left|\bar{\mathbf{u}}_1 - \bar{\mathbf{u}}_2\right|$$

$$- \gamma_2\left[\frac{\bar{u}_2}{\left|\bar{\mathbf{u}}_2\right|}c_d g_z h_2 \tan\varphi_{bed} + \left(1 - c_d\right)g_z n_b \frac{\bar{u}_2\left|\bar{\mathbf{u}}_2\right|}{h_2^{1/3}}\right]$$

$$(39)$$

Using similar procedure, the depth-averaged y-momentum component for the lower layer is obtained

$$\frac{\partial}{\partial t}\left(\gamma_2 h_2 \bar{v}_2\right) + \frac{\partial}{\partial x}\left(\gamma_2 h_2 \bar{u}_2 \bar{v}_2\right) + \frac{\partial}{\partial y}\left(\gamma_2 h_2 \bar{v}_2^2 + \frac{1}{2}k_{ap}\gamma_2 g h_2^2 + k_{ap}\gamma_1 g h_1 h_2\right) = \gamma_2(z_m)v_1(z_m)E_m + \gamma_2(z_b)v_2(z_b)E_b$$

$$+\gamma_1 g h_1 \frac{\partial z_m}{\partial y} - k_{ap}\left(\gamma_1 g h_1 + \gamma_2 g h_2\right)\frac{\partial z_b}{\partial y} + \frac{\gamma_1 g_z n_b}{h_1^{1/3}}\left(\bar{v}_1 - \bar{v}_2\right)\left|\bar{\mathbf{u}}_1 - \bar{\mathbf{u}}_2\right| \tag{40}$$

$$-\gamma_2 \left[\frac{\bar{v}_2}{|\bar{\mathbf{u}}_2|}c_d g_z h_2 \tan\varphi_{bed} + \left(1 - c_d\right)g_z n_b \frac{\bar{v}_2 |\bar{\mathbf{u}}_2|}{h_2^{1/3}}\right]$$

To address the variations of the sediment in the lower layer and the bed material, the mass conservation equations are integrated from the base to the interface using Leibniz's rule to swap the order of differentiation and integration, and then simplified by using conditions (4) and (5), which gives

$$\frac{\partial}{\partial t}\left(\gamma_2 h_2 c_d\right) + \frac{\partial}{\partial x}\left(\gamma_2 h_2 c_d \bar{u}_2\right) + \frac{\partial}{\partial y}\left(\gamma_2 h_2 c_d \bar{v}_2\right) = \gamma_2(z_b)\left(1 - p\right)E_b \tag{41}$$

where p is the sediment porosity. To describe the variation of bed terrain caused by debris flow erosion, the mass conservation equations for bed materials are needed as follows:

$$\frac{\partial z_b}{\partial t} = -E_b \tag{42}$$

References

An H, Ouyang CJ, Wang F et al (2022) Comprehensive analysis and numerical simulation of a large debris flow in the Meilong catchment. China Eng Geol 298

Aston AR (1979) Rainfall interception by eight small trees. J Hydrol 42(3–4):383–396

Audusse E, Bouchut F, Bristeau MO et al (2004) A fast and stable well-balanced scheme with hydrostatic reconstruction for shallow water flows. SIAM J Sci Comput 25(6):2050–2065

Bouchut F, Fernández-Nieto ED, Mangeney A et al (2016) A two-phase two-layer model for fluidized granular flows with dilatancy effects. J Fluid Mech 801:166–221

Bout B, Lombardo L, van Westen CJ et al (2018) Integration of two-phase solid fluid equations in a catchment model for flashfloods, debris flows and shallow slope failures. Environ Model Softw 105:1–16

Caviedes-Voullième D, García-Navarro P, Murillo J (2012) Influence of mesh structure on 2D full shallow water equations and SCS curve number simulation of rainfall/runoff events. J Hydrol 448:39–59

Chen SC, Peng SH (2006) Two-dimensional numerical model of two-layer shallow water equations for confluence simulation. Adv Water Resour 29(11):1608–1617

Church M, Jakob M (2020) What is a debris flood? Water Resour Res 56(8):e2020WR027144

Dahlquist MP, West AJ (2019) Initiation and runout of post-seismic debris flows: insights from the 2015 Gorkha earthquake. Geophys Res Lett 46(16):9658–9668

Das T, Bardossy ANDRÁS, Zehe E (2006) Influence of spatial variability of precipitation in a distributed rainfall-runoff model. IAHS Publ 303:195

Fleming RW, Ellen SD, Algus MA (1989) Transformation of dilative and contractive landslide debris into debris flows—an example from Marin County. California Eng Geol 27(1–4):201–223

Fraccarollo L, Capart H (2002) Riemann wave description of erosional dam-break flows. J Fluid Mech 461:183

Frank F, Huggel C, McArdell BW et al (2019) Landslides and increased debris-flow activity: A systematic comparison of six catchments in Switzerland. Earth Surf Process Landf 44(3):699–712

Garcia-Martino AR, Warner GS, Scatena FN et al (1996) Rainfall, runoff and elevation relationships in the Luquillo Mountains of Puerto Rico. Carib J Sci 32:413–424

George DL, Iverson RM (2014) A depth-averaged debris-flow model that includes the effects of evolving dilatancy. II. Numerical predictions and experimental tests. Proceedings of the Royal Society A: Mathematical, Physical and Engineering Sciences 470(2170):20130820

Guo XJ, Cui P, Chen XC et al (2021) Spatial uncertainty of rainfall and its impact on hydrological hazard forecasting in a small semiarid mountainous watershed. J Hydrol 595:126049

Haiden T, Pistotnik G (2009) Intensity-dependent parameterization of elevation effects in precipitation analysis. Adv Geosci 20:33–38

Han Z, Chen G, Li Y et al (2015) Numerical simulation of debris-flow behavior incorporating a dynamic method for estimating the entrainment. Eng Geol 190:52–64

Hu KH, Zhang XP, Luo H et al (2020) Investigation of the "6.17" debris flow chain at the Meilong catchment of Danba county, China. Mt Res 38(6):945–951 (In Chinese)

Huang X, Tang C (2014) Formation and activation of catastrophic debris flows in Baishui River basin, Sichuan Province, China. Landslides 11:955–967

Iverson RM, Logan M, LaHusen RG et al (2010) The perfect debris flow? Aggregated results from 28 large-scale experiments. J Geophys Res Earth Surf 115(F3)

Iverson RM, Ouyang CJ (2015) Entrainment of bed material by Earth-surface mass flows: review and reformulation of depth-integrated theory. Rev Geophys 53(1):27–58

Iverson RM, Reid ME, LaHusen RG (1997) Debris-flow mobilization from landslides. Annu Rev Earth Planet Sci 25(1):85–138

Iverson RM, Reid ME, Logan M et al (2011) Positive feedback and momentum growth during debris-flow entrainment of wet bed sediment. Nat Geosci 4(2):116–121

Jiang ZX (1988) A discussion on the mathematical model of mountain precipitation with vertical distribution. Geogr Res 1:73–78

Jiang N, Li HB, Hu YX et al (2022) Dynamic evolution mechanism and subsequent reactivated ancient landslide analyses of the "6.17" Danba sequential disasters. Bull Eng Geol Environ 81(4):149

Liang Q, Marche F (2009) Numerical resolution of well-balanced shallow water equations with complex source terms. Adv Water Resour 32(6):873–884

Liu W, He S (2016) A two-layer model for simulating landslide dam over mobile river beds. Landslides 13:565–576

Liu W, He S (2018) A two-layer model for the intrusion of two-phase debris flow into a river. Q J Eng GeolHydrogeol 51(1):113–123

Liu W, He S (2020) Comprehensive modelling of runoff-generated debris flow from formation to propagation in a catchment. Landslides 17(7):1529–1544

Liu W, He S, Li X (2015) Numerical simulation of landslide over erodible surface. Geoenvironmental Disasters 2(1):1–11

Luna BQ, Remaître A, Van Asch TW et al (2012) Analysis of debris flow behavior with a one dimensional run-out model incorporating entrainment. Eng Geol 128:63–75

McCoy SW, Kean JW, Coe JA et al (2012) Sediment entrainment by debris flows: In situ measurements from the headwaters of a steep catchment. J Geophys Res Earth Surf 117(F3)

Medina V, Hürlimann M, Bateman A (2008) Application of FLATModel, a 2D finite volume code, to debris flows in the northeastern part of the Iberian Peninsula. Landslides 5(1):127–142

Meyrat G, McArdell B, Ivanova K et al (2022) A dilatant, two-layer debris flow model validated by flow density measurements at the Swiss ill-graben test site. Landslides 19(2):265–276

Minder JR, Roe GH, Montgomery DR (2009) Spatial patterns of rainfall and shallow landslide susceptibility. Water Resour Res 45(4)

Mohrig D, Marr JG (2003) Constraining the efficiency of turbidity current generation from submarine debris flows and slides using laboratory experiments. Mar Pet Geol 20(6–8):883–899

Norio O, Ye T, Kajitani Y et al (2011) The 2011 eastern Japan great earthquake disaster: overview and comments. International Journal of Disaster Risk Science 2:34–42

Pierson TC, Scott KM (1985) Downstream dilution of a lahar: transition from debris flow to hyperconcentrated streamflow. Water Resour Res 21(10):1511–1524

Prasad R (1988) A linear root water uptake model. J Hydrol 99(3–4):297–306

Pudasaini SP, Wang Y, Hutter K (2005) Modelling debris flows down general channels. Nat Hazard 5(6):799–819

Reid ME, Iverson RM, Logan M et al (2011) Entrainment of bed sediment by debris flows: results from large-scale experiments. Ital J Eng Geol Environ 367–374

Rengers FK, McGuire LA, Kean JW et al (2016) Model simulations of flood and debris flow timing in steep catchments after wildfire. Water Resour Res 52(8):6041–6061

Rickenmann D (1999) Empirical relationships for debris flows. Nat Hazards 19:47–77

Rickenmann D, Scheidl C (2012) Debris-flow runout and deposition on the fan. In Dating torrential processes on fans and cones: methods and their application for hazard and risk assessment. Dordrecht: Springer Netherlands 75–93

Singh J, Altinakar MS, Ding Y (2015) Numerical modeling of rainfall-generated overland flow using nonlinear shallow-water equations. J Hydrol Eng 20(8):04014089

Song L, Chen M, Gao F et al (2019) Elevation influence on rainfall and a parameterization algorithm in the Beijing area. J Meteorol Res 33(6):1143–1156

Swartzendruber D (1987) A quasi-solution of Richards' equation for the downward infiltration of water into soil. Water Resour Res 23(5):809–817

Talling PJ, Peakall J, Sparks RSJ et al (2002) Experimental constraints on shear mixing rates and processes: implications for the dilution of submarine debris flows. Geological Society, London, Special Publications 203(1):89–103

Tang C, Zhu J, Ding J et al (2011) Catastrophic debris flows triggered by a 14 August 2010 rainfall at the epicenter of the Wenchuan earthquake. Landslides 8:485–497

Tang C, Zhu J, Chang M et al (2012a) An empirical–statistical model for predicting debris-flow runout zones in the Wenchuan earthquake area. Quatern Int 250:63–73

Tang C, van Asch TW, Chang M et al (2012b) Catastrophic debris flows on 13 August 2010 in the Qingping area, southwestern China: the combined effects of a strong earthquake and subsequent rainstorms. Geomorphology 139:559–576

von Hoyningen-Hune J (1983) Die interzeption des niederschlags in landwirtschaftlichen pflanzenbeständen. Schriftenreihe des Deutschen Verbandes fuer Wasserwirtschaft und Kulturbau 57:1–53

von Ruette J, Lehmann P, Or D (2014) Effects of rainfall spatial variability and intermittency on shallow landslide triggering patterns at a catchment scale. Water Resour Res 50(10):7780–7799

Wei R, Zeng Q, Davies T et al (2018) Geohazard cascade and mechanism of large debris flows in Tianmo gully, SE Tibetan Plateau and implications to hazard monitoring. Eng Geol 233:172–182

Yan Y, Cui Y, Liu D et al (2021) Seismic signal characteristics and interpretation of the 2020 "6.17" Danba landslide dam failure hazard chain process. Landslides 18:2175–2192

Yin M, Rui Y (2018) Laboratory study on submarine debris flow. Mar Georesour Geotechnol 36(8):950–958

Zhao B, Zhang H, Hongjian L et al (2021) Emergency response to the reactivated Aniangzhai landslide resulting from a rainstorm-triggered debris flow, Sichuan Province. China Landslides 18(3):1115–1130

Zhu H, Zhang LM, Garg A (2018) Investigating plant transpiration-induced soil suction affected by root morphology and root depth. Comput Geotech 103:26–31

Wei Liu · Siming He (✉)
State Key Laboratory of Mountain Hazards and Engineering Resilience, Institute of Mountain Hazards and Environment, Chinese Academy of Sciences, Chengdu 610041, China
Email: hsm@imde.ac.cn